



Recognition and inhibition of SARS-CoV-2 by humoral innate immunity pattern recognition molecules

Matteo Stravalaci^{1,2,15}, Isabel Pagani^{3,15}, Elvezia Maria Paraboschi^{1,2}, Mattia Pedotti⁴, Andrea Doni¹, Francesco Scavello¹, Sarah N. Mapelli¹, Marina Sironi¹, Chiara Perucchini¹, Luca Varani⁴, Milos Matkovic⁴, Andrea Cavalli^{4,5}, Daniela Cesana⁶, Pierangela Gallina⁶, Nicoletta Pedemonte⁷, Valeria Capurro⁷, Nicola Clementi⁸, Nicasio Mancini⁸, Pietro Invernizzi^{9,10}, Rafael Bayarri-Olmos¹¹, Peter Garred¹¹, Rino Rappuoli^{12,13}, Stefano Duga^{1,2}, Barbara Bottazzi¹, Mariagrazia Ugucioni^{2,4}, Rosanna Asselta^{1,2}, Elisa Vicenzi³✉, Alberto Mantovani^{1,2,14}✉ and Cecilia Garlanda^{1,2}✉

The humoral arm of innate immunity includes diverse molecules with antibody-like functions, some of which serve as disease severity biomarkers in coronavirus disease 2019 (COVID-19). The present study was designed to conduct a systematic investigation of the interaction of human humoral fluid-phase pattern recognition molecules (PRMs) with severe acute respiratory syndrome coronavirus 2 (SARS-CoV-2). Of 12 PRMs tested, the long pentraxin 3 (PTX3) and mannose-binding lectin (MBL) bound the viral nucleocapsid and spike proteins, respectively. MBL bound trimeric spike protein, including that of variants of concern (VoC), in a glycan-dependent manner and inhibited SARS-CoV-2 in three in vitro models. Moreover, after binding to spike protein, MBL activated the lectin pathway of complement activation. Based on retention of glycosylation sites and modeling, MBL was predicted to recognize the Omicron VoC. Genetic polymorphisms at the MBL2 locus were associated with disease severity. These results suggest that selected humoral fluid-phase PRMs can play an important role in resistance to, and pathogenesis of, COVID-19, a finding with translational implications.

SARS-CoV-2 is a highly pathogenic coronavirus and the causative agent of the current COVID-19 pandemic^{1–3}. Innate immunity is credited to play a fundamental role in this condition and may eradicate the infection in its early phases before adaptive immune responses take place. In severe forms of the disease, uncontrolled activation of innate and adaptive immunity results in hyperinflammatory responses, which affect the lung and blood vessels, contributing to acute respiratory distress syndrome, shock and multiorgan failure⁴.

Innate immunity includes a cellular arm and a humoral arm⁵. The humoral arm consists of soluble PRMs belonging to different families, which include collectins (for example, MBL), ficolins, pentraxins (C-reactive protein (CRP), serum amyloid P component (SAP) and PTX3) and C1q^{5–7}. Humoral PRMs represent functional ancestors of antibodies (ante-antibodies), as they recognize microbial components and eliminate pathogens with common mechanisms that include agglutination, neutralization, activation of the complement cascade and opsonization facilitating phagocytosis⁵.

Investigations of the role of humoral innate immunity in viral sensing have shown that collectins bind to envelope glycoproteins on enveloped viruses, including influenza A virus, human immunodeficiency virus, hepatitis C virus and herpes simplex virus, and to the non-enveloped rotavirus⁶. This interaction may result in opsonization, agglutination, inhibition of viral fusion and entry or complement activation, generally leading to inhibition of infection⁶. Among pentraxins, the long pentraxin PTX3 has been shown to interact with H3N2-subtype influenza virus type A by interacting with viral envelope hemagglutinin and neuraminidase glycoproteins through a sialic acid residue on its glycosidic moiety⁸, with cytomegalovirus (CMV)⁹ and with the coronavirus murine hepatitis virus strain 1 (ref. ¹⁰), preventing viral infection.

Several lines of evidence, including genetic associations, indicate that cellular innate immunity and related cytokines and chemokines play a key role in SARS-CoV-2 recognition, antiviral resistance and, at later stages, severe disease^{11–14}. By contrast, little information is available concerning the role of the humoral

¹IRCCS Humanitas Research Hospital, Milan, Italy. ²Department of Biomedical Sciences, Humanitas University, Milan, Italy. ³Viral Pathogenesis and Biosafety Unit, IRCCS San Raffaele Scientific Institute, Milan, Italy. ⁴Institute for Research in Biomedicine, Università della Svizzera italiana (USI), Bellinzona, Switzerland. ⁵Swiss Institute of Bioinformatics, Lausanne, Switzerland. ⁶San Raffaele Telethon Institute for Gene Therapy (SR-Tiget), IRCCS, San Raffaele Scientific Institute, Milan, Italy. ⁷UOC Genetica Medica, IRCCS Istituto Giannina Gaslini, Genova, Italy. ⁸Laboratory of Microbiology and Virology, IRCCS Scientific Institute and Vita-Salute San Raffaele University, Milan, Italy. ⁹Division of Gastroenterology, Center for Autoimmune Liver Diseases, Department of Medicine and Surgery, University of Milano-Bicocca, Monza, Italy. ¹⁰European Reference Network on Hepatological Diseases (ERN RARE-LIVER), San Gerardo Hospital, Monza, Italy. ¹¹Laboratory of Molecular Medicine, Department of Clinical Immunology, Section 7631, Rigshospitalet, Copenhagen University Hospital, København, Denmark. ¹²Monoclonal Antibody Discovery Lab, Fondazione Toscana Life Sciences, Siena, Italy. ¹³Faculty of Medicine, Imperial College London, London, UK. ¹⁴The William Harvey Research Institute, Queen Mary University of London, Charterhouse Square, London, UK. ¹⁵These authors contributed equally: Matteo Stravalaci, Isabel Pagani. ✉e-mail: vicenzi.elisa@hsr.it; alberto.mantovani@humanitasresearch.it; cecilia.garlanda@humanitasresearch.it

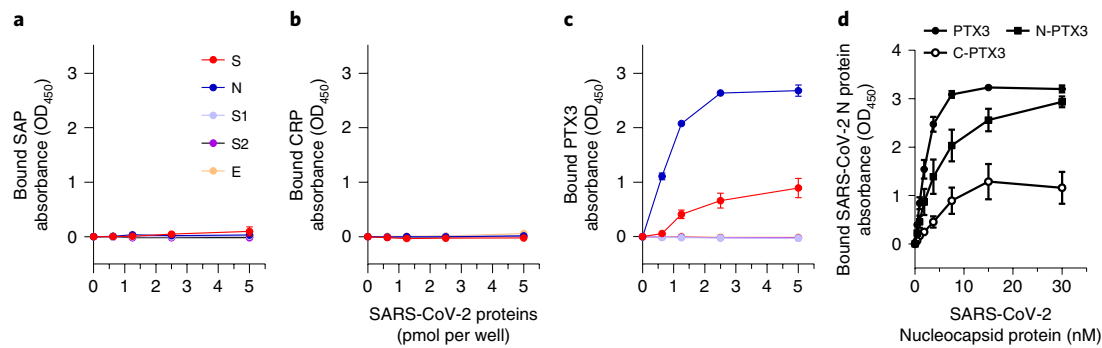


Fig. 1 | Interaction between pentraxins and SARS-CoV-2 proteins. a–c, Recombinant His tag SARS-CoV-2 proteins (spike active trimer (S), S1, S2, nucleocapsid (N) and envelope (E); the legend refers to **a–c**) were immobilized on 96-well nickel-coated plates at different concentrations. Fixed concentrations of SAP (**a**), CRP (**b**) and PTX3 (**c**) were incubated over the captured viral proteins. Bound pentraxins were detected by enzyme-linked immunosorbent assay (ELISA) with specific primary antibodies. **d**, Full-length PTX3 or the N- or C-terminal domains were captured on 96-well plates. Biotinylated SARS-CoV-2 nucleocapsid protein was incubated at different concentrations. Bound nucleocapsid was detected by ELISA using horseradish peroxidase (HRP)-conjugated streptavidin. All data are presented as mean \pm s.e.m.; $n=3$ independent experiments performed in duplicate; OD₄₅₀, optical density at 450 nm.

arm of innate immunity in COVID-19 resistance and pathogenesis in spite of the clinical prognostic significance of CRP and PTX3 (refs. ^{15,16}).

The present study was designed to conduct a systematic investigation of the interaction of the human humoral PRMs with SARS-CoV-2. We found that PTX3 and MBL bound the SARS-CoV-2 nucleocapsid protein and spike protein, respectively. MBL recognized VoC, had antiviral activity and activated the complement lectin pathway. Genetic polymorphisms at the *MBL2* locus were associated with disease severity. Thus, selected fluid-phase PRMs (ante-antibodies) play an essential role in resistance to and pathogenesis of COVID-19, a finding with translational implications.

Results

Interaction of humoral PRMs with SARS-CoV-2 proteins. To study the role of humoral PRMs in recognizing SARS-CoV-2, we first investigated the interaction between recombinant human humoral innate immunity molecules and SARS-CoV-2 proteins using a solid-phase binding assay. We first analyzed pentraxins, and we did not observe specific binding of CRP or SAP to any of the SARS-CoV-2 proteins tested (spike protein subunit S1, spike protein subunit S2, spike protein active trimer, nucleocapsid and envelope protein) (Fig. 1a,b). By contrast, PTX3 bound specifically and in a dose-dependent manner to the nucleocapsid protein, one of the most abundant proteins of SARS-CoV-2 (ref. ¹⁷) (Fig. 1c). We validated this result by confirming the binding of PTX3 with SARS-CoV-2 nucleocapsid protein obtained from different sources (Extended Data Fig. 1). PTX3 is a multimeric glycoprotein arranged in an octameric structure. Each protomer comprises a flexible N-terminal region and a C-terminal domain with homology to the short pentraxin family⁵. To define which portion of the molecule was involved in the interaction, we compared the binding of full-length PTX3 and its N-terminal or C-terminal domains to SARS-CoV-2 nucleocapsid protein. Results indicate that PTX3 interacts with SARS-CoV-2 nucleocapsid protein mainly through its N-terminal domain, although with lower affinity than full-length PTX3 (Fig. 1d).

We next investigated the interaction between PRMs of the classical pathway and the lectin pathway of complement (C1q and the collectin MBL, respectively) and the viral proteins. C1q did not interact with any protein tested (Fig. 2a). By contrast, human MBL bound to SARS-CoV-2 spike protein (Wuhan strain¹, active trimer) but not to the individual SARS-CoV-2 spike protein subunits S1 (containing the receptor-binding domain (RBD)) and

S2 (containing the membrane fusion domain) (Fig. 2b). We validated these data by analyzing the binding of MBL to different recombinant SARS-CoV-2 spike proteins obtained from different sources or produced in-house either in HEK293 cells, CHO cells or insect cells (Fig. 2c). All these preparations were bound by MBL, although with some differences. Notably, we did not observe binding when we tested a non-covalent trimer of the SARS-CoV-2 spike protein. These results indicate that a native-like structure of the SARS-CoV-2 spike protein (presumably in the trimeric conformation) is indispensable for MBL recognition.

MBL is a member of the collectin family, a class of PRMs composed of a Ca²⁺-type lectin domain (also called carbohydrate recognition domain (CRD)) and a collagen-like domain⁶. Thus, we analyzed the interaction of SARS-CoV-2 spike protein with other collectins involved in innate immunity, such as collectin-10, collectin-11 and collectin-12 (also known as CL-L1/CL-10, CL-K1/CL-11 and CL-P1/CL-12) and the pulmonary surfactant proteins SP-A and SP-D. We also extended the analysis to recombinant ficolin-1, ficolin-2 and ficolin-3, a family of proteins known to activate the complement lectin pathway and structurally related to MBL. In contrast with MBL, collectin-10, collectin-11, collectin-12, SP-A, SP-D and ficolins did not bind to SARS-CoV-2 spike protein (Fig. 2d,e and Extended Data Fig. 1), indicating that recognition of the spike protein is unique to MBL.

We further characterized the interaction of SARS-CoV-2 spike protein with MBL by surface plasmon resonance (SPR). Different concentrations of recombinant SARS-CoV-2 spike protein or RBD domain were flowed onto MBL immobilized on the biosensor surface. Trimeric SARS-CoV-2 spike protein formed a stable calcium-dependent complex with nanomolar affinity ($K_d=34$ nM), whereas MBL did not bind the isolated RBD (Fig. 2f and Extended Data Fig. 2), confirming the results obtained using the S1 subunit.

These results indicate that of 12 humoral PRMs tested in a solid-phase binding assay, PTX3 and MBL bound the SARS-CoV-2 nucleocapsid protein and spike protein, respectively.

Interaction of MBL with spike-pseudotyped lentivirus. To mimic the interaction between MBL and SARS-CoV-2 spike protein in its physiological conformation in the viral envelope, we investigated the binding of viral particles of SARS-CoV-2 spike protein pseudotyped on a lentivirus vector to MBL-coated plates. The interaction was determined by lysing the bound pseudovirus and measuring the released lentiviral vector p24 core protein by ELISA. While lentiviral control particles pseudotyped with the vesicular stomatitis virus (VSV)-g glycoprotein (VSV-pseudovirus) did not result in

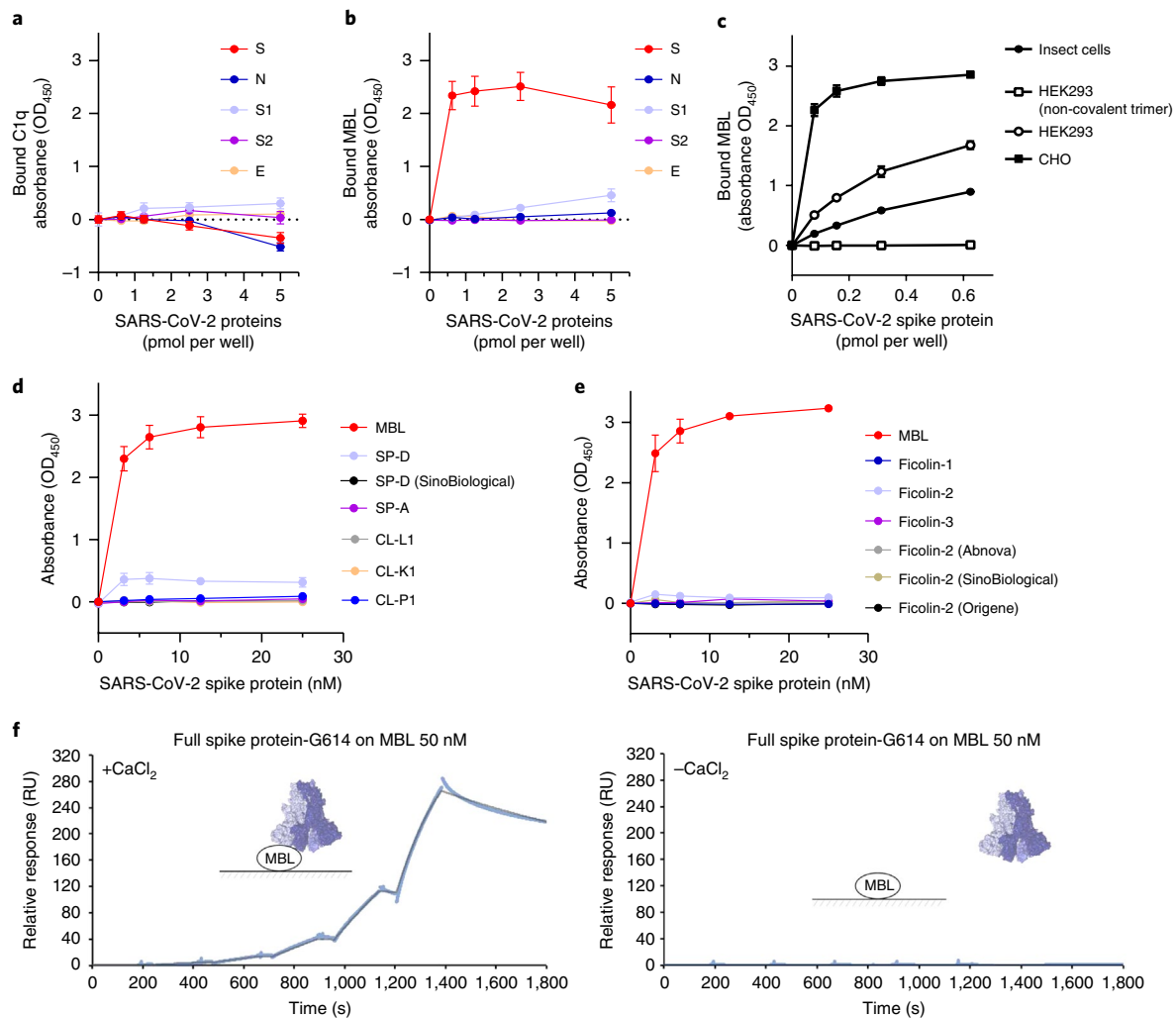


Fig. 2 | Interaction of C1q, MBL, ficolins and surfactant proteins with SARS-CoV-2 proteins. **a–c**, Recombinant His tag SARS-CoV-2 proteins (spike active trimer (S), S1, S2, nucleocapsid (N) and envelope (E)) were immobilized on 96-well nickel-coated plates at different concentrations. Fixed concentrations of C1q (**a**) or MBL (**b**) were incubated over the captured viral proteins. Recombinant SARS-CoV-2 spike proteins tested were expressed in different cell types (**c**). MBL (2 μg ml⁻¹; 6.7 nM) was incubated over the captured viral proteins. In **a–c**, bound proteins were detected by ELISA with specific primary antibodies. Data in **a** and **b** are presented as mean ± s.e.m.; *n* = 3 independent experiments performed in duplicate. Data in **c** are presented as mean ± s.e.m.; *n* = 2 independent experiments, one performed in duplicate and one in triplicate. **d,e**, MBL-, CL-L1, CL-K1, CL-P1-, SP-D- and SP-A-coated plates or (**d**) ficolin-1-, ficolin-2- and ficolin-3-coated plates (**e**) were incubated with various concentrations of biotinylated SARS-CoV-2 spike protein. Bound spike protein was detected by ELISA with HRP-conjugated streptavidin (mean ± s.e.m.; *n* = 3 independent experiments in duplicate). **f**, SPR shows binding of recombinant full spike protein trimer to immobilized MBL (dissociation constant (K_d) = 34 nM, left). No binding was detected in the absence of CaCl₂ (right); RU, resonance units.

any binding, those exposing the SARS-CoV-2 spike protein showed specific interaction with MBL (Fig. 3a). These data strongly suggest that MBL can also interact with the SARS-CoV-2 spike protein exposed on the virus surface.

MBL interacts with glycosidic sites of the SARS-CoV-2 spike protein. The SARS-CoV-2 spike protein is highly glycosylated, as recently described in ref. ¹⁸. Of the 22 N-glycosylation sites, 8 contain oligomannose-type glycans, which could be interaction sites for the MBL CRD. To address this possibility, we performed a solution-based competition assay with D-mannose and N-acetyl-glucosamine, two specific ligands of the lectin. D-Mannose and N-acetyl-glucosamine inhibited MBL binding to the spike protein (Fig. 3b), thus confirming the Ca²⁺-dependent interaction between the MBL lectin domain and the glycosidic sites exposed by the spike protein. D-Glucose, a non-specific ligand of MBL, inhibited the interaction only at higher

concentrations (Fig. 3b). Based on the alignment of the MBL crystal structure with mannose molecules (Fig. 3c), we identified 14 putative binding sites on the spike protein (Fig. 3d). Next, we considered sites having a high (>80%) oligomannosylation occupancy¹⁸. This analysis provided two possible MBL-binding sites, namely N603, N801 and N1074, all on the same spike chain, or N603, N1074 and N709, with N709 on a neighboring chain (Fig. 3e). Interestingly, in both cases, the hypothesized MBL-binding sites span across the S1 and S2 regions of the spike protein (Fig. 3f), providing hints to a possible inhibition mechanism. These data indicate that the glycosylation state of the SARS-CoV-2 spike protein is important for its interaction with MBL.

Interaction of MBL with spike protein from VoC. We then tested whether MBL recognized spike proteins from VoC. First, we analyzed whether the reported mutations affected the known 22

glycosylation sites of each protomer. Fig. 3g shows a schematic representation of the 22 positions of N-linked glycosylation sequons and of 66 known mutations of VoC and variants of interest, including the recently added Epsilon, Lambda and Omicron variants, indicating that none of these mutations involve the glycosylation sites and suggesting that MBL could interact with the variants with the same affinity. In agreement with our binding assays, no MBL target sites are expected in the RBD. Interestingly, the predicted MBL-binding sites are conserved in the Omicron VoC, as shown in the spike–MBL complex model (Extended Data Fig. 3). We assessed by solid-phase assay the interaction of MBL with the SARS-CoV-2 D614G spike trimeric protein, the B.1.1.7 variant (Alpha; emerged in the United Kingdom), the B.1.1.28 or P.1 variant (Gamma; emerged in Brazil), the B.1.351 variant (Beta; emerged in South Africa) and the B.1.617.2 variant (Delta; emerged in India), which is currently a major concern worldwide (Fig. 3h). In agreement with the *in silico* analysis, MBL efficiently bound the VoC spike proteins tested. These results indicate that the potential MBL-binding sites are conserved in the VoC spike proteins, and the affinity of the interaction with MBL is not affected by these mutations.

Complement lectin pathway activation. Next, we tested whether the interaction of MBL with spike protein could activate the complement lectin pathway. We incubated SARS-CoV-2 spike protein-coated plates with human serum or C1q-, C4- or C3-depleted serum, and we assessed the deposition of C5b-9. Incubation with either normal human serum or C1q-depleted serum resulted in complement deposition mediated by SARS-CoV-2 spike protein (Fig. 3i, left). Conversely, incubation with a serum depleted of C4 strongly reduced C5b-9 deposition, with levels comparable to those observed with heat-inactivated serum or C3-depleted serum. Reconstitution of C4-depleted serum with purified C4 restored C5b-9 deposition levels similar to those observed with normal human serum. To further address the role of MBL in SARS-CoV-2 spike protein-mediated complement activation, we assessed C5b-9 deposition by incubating normal human serum or MBL-immunodepleted serum over captured SARS-CoV-2 spike protein either as active or non-covalent trimer (Fig. 3i, right). In agreement with the binding data, no complement deposition was observed with the non-covalent trimeric spike protein. Notably, immunodepletion of MBL from human serum resulted in a significant reduction in C5b-9 deposition, which could be fully reverted by the addition of rhMBL (Fig. 3i, right). These data clearly indicate that SARS-CoV-2 spike protein, by interacting with MBL, activates the complement lectin pathway.

SARS-CoV-2 inhibition by MBL. To validate the relevance of the interaction between MBL and SARS-CoV-2 spike protein, we investigated whether MBL inhibited SARS-CoV-2 entry in susceptible

cells. We first tested the effect of MBL and other soluble PRMs (ten-fold serial dilution, from 0.01 to 10 $\mu\text{g ml}^{-1}$) on the entry of viral particles of SARS-CoV-2 spike protein pseudotyped on a lentivirus vector in 293T cells overexpressing angiotensin-converting enzyme 2 (ACE2). Among the soluble PRMs tested, MBL was found to be the only molecule with anti-SARS-CoV-2 activity. Spike-mediated viral entry was inhibited by 90% at the highest concentration of 10 $\mu\text{g ml}^{-1}$ (34 nM), with a half-maximum effective concentration (EC_{50}) value of approximately 0.5 $\mu\text{g ml}^{-1}$ (1.7 nM) (Fig. 4a). As a control, entry of lentiviral particles pseudotyped with the VSV-g glycoprotein was not inhibited by MBL (Fig. 4a).

We next tested the antiviral activity of MBL on SARS-CoV-2 infection of lung epithelial models relevant to human infections. Among a number of lung-derived epithelial cell lines, Calu-3 (human lung adenocarcinoma) cells have been shown to be permissive to SARS-CoV-2 infection¹⁹. SARS-CoV-2 (D614G variant; MOI = 0.1 and 1) was preincubated in complete medium containing different concentrations of MBL (0.01–10 $\mu\text{g ml}^{-1}$; 0.034–34 nM) before incubation with Calu-3 cells. After 48 and 72 h, the infectivity of SARS-CoV-2 present in cell culture supernatants was determined by a plaque-forming assay in monkey-derived Vero cells. Vero cells are a handy cell line used worldwide as it is devoid of the interferon (IFN) response²⁰ and, for this reason, is highly supportive of virus replication. MBL showed a concentration-dependent inhibition of SARS-CoV-2 infection of Calu-3 cells at an MOI of 0.1 and 1 (Extended Data Fig. 4a) that was statistically significant at 1 and 10 $\mu\text{g ml}^{-1}$ (3.4 and 34 nM) 72 h after infection. When both virus and cells were preincubated with the same concentrations of MBL (0.01–10 $\mu\text{g ml}^{-1}$; 0.034–34 nM), the antiviral activity increased significantly from 0.1 $\mu\text{g ml}^{-1}$ (0.34 nM) to the top concentration of 10 $\mu\text{g ml}^{-1}$ (34 nM) 72 h after infection (Fig. 4b and Extended Data Fig. 4b). The calculated EC_{50} was 0.08 $\mu\text{g ml}^{-1}$ (0.27 nM) at 72 h after infection. Notably, MBL showed a concentration-dependent inhibition of infection of Calu-3 cells also by the SARS-CoV-2 B.1.1.7 (Alpha) variant at an MOI of 0.1 (Fig. 4c) and an MOI of 0.01 (Extended Data Fig. 4c) and by the B.1.351 (Beta) variant at an MOI of 0.1 (Fig. 4d), the P.1 (Gamma) variant at an MOI of 0.1 (Fig. 4e) and the B.1.617.2 (Delta) variant at an MOI of 0.1 (Fig. 4f).

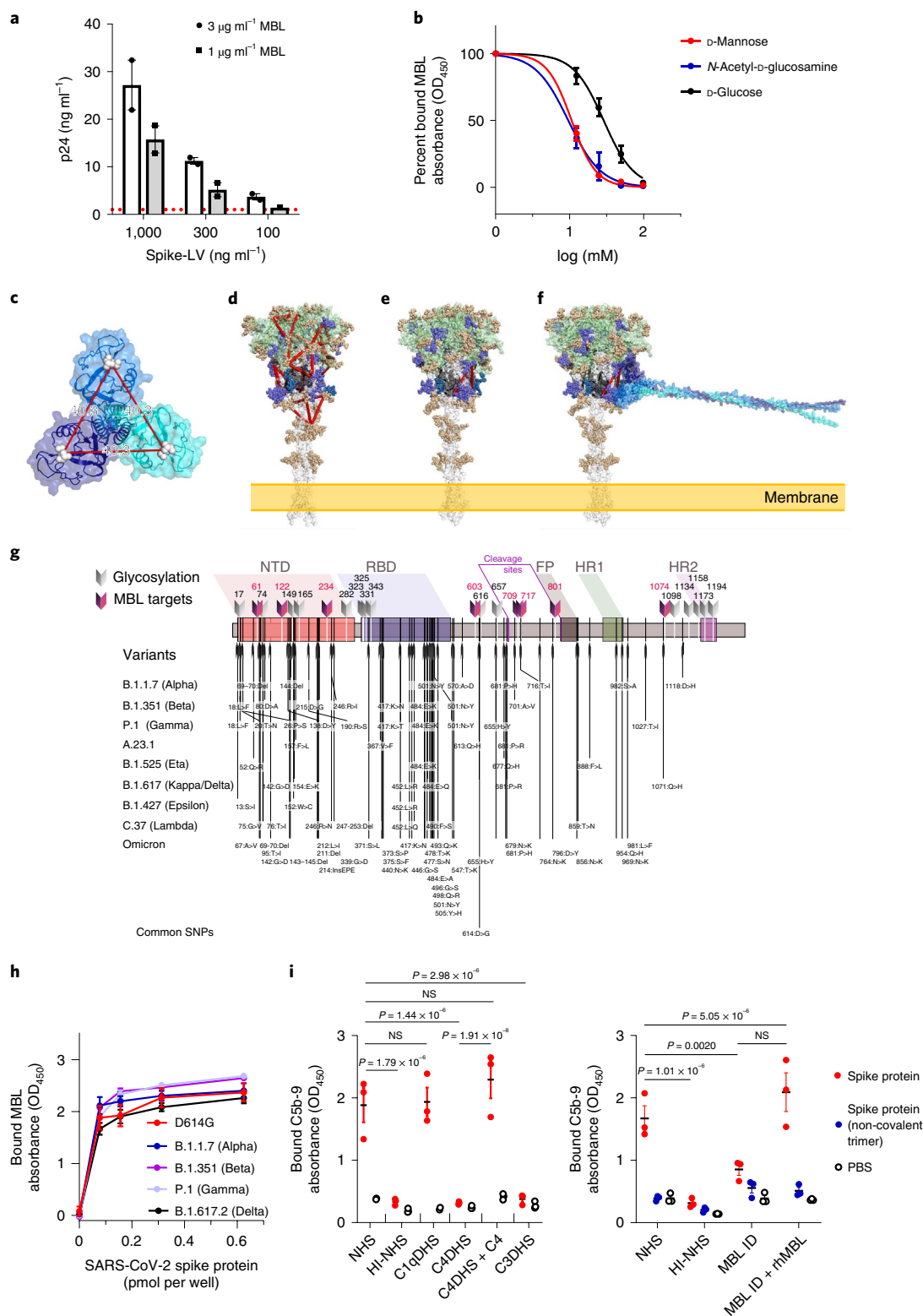
Furthermore, a three-dimensional (3D) human bronchial epithelial cell (HBEC) model was used to test whether MBL inhibited SARS-CoV-2 replication. SARS-CoV-2 production at the epithelial apical surface increased sharply at 48 h after infection (not shown), reaching $48 \times 10^6 \pm 6 \times 10^6$ PFU ml^{-1} (mean \pm s.e.m.) 72 h after infection. Treatment of HBECs with MBL decreased viral production to $4 \times 10^6 \pm 0.8 \times 10^6$ PFU ml^{-1} 72 h after infection at the highest concentration of 50 $\mu\text{g ml}^{-1}$ (170 nM) (Fig. 5a). By contrast, PTX3 treatment was ineffective at inhibiting virus production (Extended Data Fig. 4d). We then assessed whether MBL affected inflammatory responses in HBEC following SARS-CoV-2

Fig. 3 | Interaction of MBL with SARS-CoV-2 spike protein through its CRD. **a**, Binding of MBL to spike protein (Spike-LV) or VSV-g-pseudotyped lentivirus (red dotted line). Data are presented as mean \pm s.e.m.; $n = 2$ independent experiments performed with two to six technical replicates. **b**, Binding of MBL to spike protein, alone or in the presence of D-mannose, N-acetyl-glucosamine or D-glucose. Data are presented as mean \pm s.e.m.; $n = 4$ independent experiments. **c**, Trimeric MBL2 model showing the distance (approximately 40 Å) between the binding sites of mannose (white spheres). **d**, Fourteen mannose-binding sites (red triangles) imposed onto spike protein, where the S1 region (1–685) is green, the beginning of the S2 region (686–815) is black and the S2' region is white. **e**, Putative binding site of MBL2. The structure is posed with the highest site-specific probability to be glycosylated with oligomannose. **f**, The spike–MBL complex. Glycosylation sites are colored according to the oligomannose content: gold, <60%; purple, >80% up until the S2' region; blue, >80% in the S2' region. **g**, Schematic representation of glycosylation sites and nucleotide substitutions in the variant strains identified to date. Oligomannose-glycosylated sites are shown. Single-nucleotide polymorphisms (SNPs) common to all variants are in bold; NTD, N-terminal domain; FP, fusion peptide; HR1 and HR2, heptad repeat 1 and 2; cleavage sites are reported. **h**, Binding of MBL to SARS-CoV-2 spike protein variants. Data are presented as mean \pm s.e.m.; $n = 2$ independent experiments performed in triplicate. **i**, Membrane attack complex (MAC) (C5b-9) deposition on spike protein. Data are presented as mean \pm s.e.m.; $n = 3$ of three independent experiments performed in triplicate. Statistical analysis was calculated by two-way analysis of variance (ANOVA), followed by Tukey's multiple comparison test; NHS, normal human serum; HI-NHS, heat-inactivated normal human serum; C1qDHS, C1q-depleted human serum; C4DHS, C4-depleted human serum; C3DHS, C3-depleted human serum; MBL ID, MBL-immunodepleted serum; rhMBL, recombinant human MBL.

infection under these experimental conditions. MBL treatment inhibited the production of interleukin-8 (IL-8) and CXCL5, two chemokines involved in myeloid cell recruitment and activation (Extended Data Fig. 4e).

We then evaluated the occurrence of MBL–spike protein interaction in SARS-CoV-2-infected HBECs by confocal microscopy. MBL colocalized with SARS-CoV-2 spike protein in infected cells

(Fig. 5b,c). In 3D-rendered images of the HBEC cultures (Fig. 5d and Supplementary Video 1), colocalization was preferentially associated with the apical side of cytokeratin 14 (Krt14)-positive cells. Evidence of the interaction between MBL and SARS-CoV-2 spike protein in infected HBECs at the molecular scale (<100-nm *xy* spatial resolution) were also obtained in STED-based super-resolution microscopy (Fig. 5e).



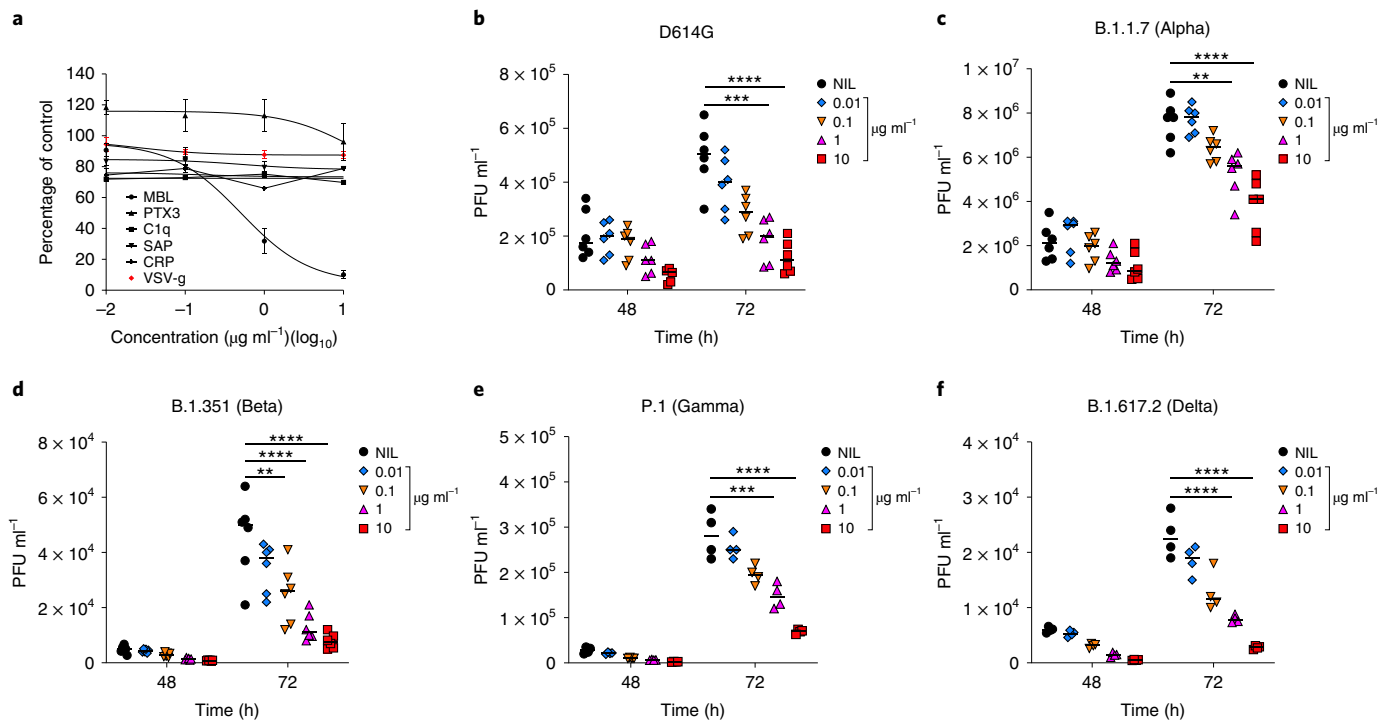


Fig. 4 | Inhibition of SARS-CoV-2 infection by MBL. **a**, Entry of lentiviral particles pseudotyped with SARS-CoV-2 spike protein in 293T cells overexpressing ACE2 in the presence of tenfold serial dilutions of humoral innate immunity PRMs (from 0.01 to 10 $\mu\text{g ml}^{-1}$). As a control, entry of lentiviral particles pseudotyped with the VSV-g glycoprotein was tested in parallel in the presence of MBL. The percentage of control was calculated as the ratio of green fluorescent protein (GFP)-positive cells in the presence of humoral PRMs to the GFP-positive cells in the absence of humoral PRMs. Data are presented as means \pm s.e.m.; $n=3$ independent experiments in triplicate, with the curves representing a three-parameter dose-response model. **b–f**, Inhibition of the infectivity of the D614G (isolate EPI_ISL_413489) (**b**), B.1.1.7 (Alpha) (**c**), B.1.351 (Beta) (**d**), P.1 (Gamma) (**e**) and B.1.617.2 (Delta) (**f**) SARS-CoV-2 variants in Calu-3 cells. SARS-CoV-2 (multiplicity of infection (MOI) = 0.1) and Calu-3 cells were preincubated in complete medium containing different concentrations of MBL (0.01–10 $\mu\text{g ml}^{-1}$; 0.034–34 nM) before infection. At 48 and 72 h after infection, the infectivity of SARS-CoV-2 present in cell culture supernatants was determined by a plaque-forming assay in Vero cells; NIL, no MBL; PFU, plaque-forming units. Data are presented as mean values; $n=3$ independent cell culture experiments in duplicate (**b–d**) or $n=2$ independent cell culture experiments in duplicate (**e** and **f**); *** $P=5.49 \times 10^{-4}$ and **** $P=6.38 \times 10^{-5}$ (**b**); ** $P=0.0072$ and **** $P=5.57 \times 10^{-5}$ (**c**); ** $P=0.0065$, **** $P=4.91 \times 10^{-5}$ NIL versus 1 and **** $P=7.14 \times 10^{-6}$ NIL versus 10 (**d**); *** $P=3.40 \times 10^{-4}$ and **** $P=6.31 \times 10^{-6}$ (**e**); **** $P=5.68 \times 10^{-5}$ NIL versus 1 and **** $P=4.04 \times 10^{-6}$ NIL versus 10 (**f**). Statistical analysis was determined by two-way ANOVA, followed by Bonferroni's multiple comparison test.

These results indicate that MBL inhibits SARS-CoV-2 infection of a human lung-derived epithelial cell line and primary bronchial cells, reduces the induced inflammatory response and colocalizes with SARS-CoV-2 spike protein in infected cells.

MBL2 variants are associated with severe COVID-19. Human MBL is encoded by the *MBL2* gene, which contains polymorphic variants both in the regulatory and structural part of the gene. These variants are associated with the serum concentration of the protein²¹. *MBL2* genetic variants have been shown to correlate with increased susceptibility to selected infections, including SARS²². To explore the significance of our in vitro results in the frame of the COVID-19 pandemic, we investigated the possible association of *MBL2* polymorphisms with severe COVID-19 with respiratory failure in an Italian cohort of 332 infected and 1,668 healthy individuals (general population). We initially focused on six SNPs known to be associated with MBL protein levels (Table 1)^{23–26}. We observed a significant difference only in the frequency of the *rs5030737*-A allele between infected and healthy individuals (7.7% and 6.0%, respectively; odds ratio (OR) = 1.43, 95% confidence interval (95% CI) = 1.00–2.05, $P=0.049$; Table 1), which, however, did not pass multiple testing correction. We also verified the distribution of infected and healthy individuals carrying these functional SNPs in biallelic conditions by specifically focusing on the three missense

variants and on the promoter SNP known to confer the strongest effect on *MBL2* expression (*rs7096206*). In agreement with in vitro functional assays, a significant predisposing effect was observed in those individuals carrying two disruptive alleles among *rs5030737*, *rs1800450* and *rs1800451* (OR = 2.09, 95% CI = 1.18–3.71, $P=0.011$; Supplementary Table 1).

When we compared the frequencies of haplotypes determined by all six SNPs, we found that the CCGCC haplotype frequency was significantly decreased in individuals with severe COVID-19 (26.7% in infected individuals and 30.4% in healthy individuals). This haplotype shows a protective effect (OR = 0.78, 95% CI = 0.65–0.95, $P=0.025$; Supplementary Table 2), consistent with the lack of the *rs5030737*-A allele, which is only present in the CCAGCC haplotype (OR = 1.38, 95% CI = 1.00–1.90, $P=0.078$; Supplementary Table 2).

Although borderline, these first association results encouraged us to investigate the 1-megabase (Mb)-long genomic region encompassing the *MBL2* gene systematically. To this aim, we performed single-SNP and haplotype-based association analyses using genotyped/imputed data on 3,425 polymorphisms. Single-SNP association analysis revealed three suggestive signals (*rs150342746*, OR = 3.47, 95% CI = 1.81–6.68, $P=1.86 \times 10^{-4}$; *rs10824845*, OR = 1.76, 95% CI = 1.30–2.39, $P=2.91 \times 10^{-4}$; *rs11816263*, OR = 1.42, 95% CI = 1.17–1.73, $P=3.47 \times 10^{-4}$; Table 2 and

Fig. 6a,b), whereas haplotype-based analysis disclosed seven haplotypes of different lengths, from 2 to 24 SNPs, strongly associated with severe COVID-19 (all passing the correction for multiple tests; Fig. 6 and Supplementary Table 3). Among them, the one composed of polymorphisms *rs10824844*–*rs10824845* incorporates one of the two top markers evidenced by the single-SNP association analysis and is present in 12.2% of infected individuals and 6.9% of healthy individuals (TA haplotype, OR=1.88, 95% CI=1.44–2.45, $P=1.04 \times 10^{-5}$; Supplementary Table 3). Hence, we performed a meta-analysis based on the *rs10824845* polymorphism by including the Geisinger Health System (GHS) study of individuals with COVID-19; this resulted in a pooled OR=1.32, 95% CI=1.15–1.52, $P=9.12 \times 10^{-5}$ (Supplementary Table 4). Notably, the *rs10824845* polymorphism points to a regulatory region characterized by the presence of an enhancer (GH10J052964), described as a distant modulator of *MBL2* gene expression. This regulatory element is active in HepG2 cells (hepatocytes) and M0 (from venous blood) and M1 (from cord and venous blood) macrophages (data from the GeneHancer database²⁷, available through <http://www.genecards.org/>).

We also interrogated the Regeneron database²⁸ to analyze the role of rare genetic variants in the *MBL2* gene in the predisposition to severe COVID-19. We depict the burden analyses both on singletons and on rare damaging variants with MAF < 1% (Supplementary Table 5). The meta-analysis was focused on the European population and evidenced the significant contribution of singleton variants. This was observed when only loss-of-function variants were considered (M1 analysis, OR=32.05, 95% CI=2.27–452.7, $P=0.010$; Supplementary Table 5) and when both loss-of-function and missense variants, predicted as damaging by five algorithms, were analyzed (M3 analysis, OR=23.6, 95% CI=3.44–162.09, $P=0.0013$; Supplementary Table 5).

Moreover, the same database reports a significant association for the *rs35668665* polymorphism both with susceptibility to COVID-19 (OR=4.11, GHS cohort) and with severity of symptoms (OR=7.91, UK BioBank cohort). Interestingly, this variant maps in correspondence of the last nucleotide of the *MBL2* exon 1, thus possibly interfering with the splicing process.

Finally, we measured MBL plasma concentrations at hospital admission in 40 individuals from the Humanitas Clinical and Research Center cohort and correlated them to *MBL2* genetic variants. We first focused on the three missense variants (functional SNPs *rs5030737*, *rs1800450* and *rs1800451*) and grouped individuals carrying at least one alternative allele (allele 0) compared to those carrying the wild-type allele. We observed a significantly lower MBL plasma concentration ($P=6.2 \times 10^{-8}$) in individuals carrying at least one alternative allele (allele 0) compared to those carrying the wild-type allele (Fig. 6c). Then we analyzed the impact of the *rs10824845* SNP by stratifying the same individuals according to their genotype. We observed a reduction of MBL concentration in

heterozygous individuals, although not significant (1.2-fold decrease in heterozygous; $P=0.11$). However, when considering the contribution of A/0 alleles, a clear genotype-dependent modulation of MBL concentrations emerged ($P=1.1 \times 10^{-6}$; Fig. 6d). Altogether, these analyses indicate that *MBL2* genetic variants are associated with COVID-19 severity and impact on protein abundance of this ‘ante-antibody’.

Discussion

Among the 12 fluid-phase PRMs tested in this study, only PTX3 and MBL bound SARS-CoV-2 virus components. PTX3 recognized the viral nucleocapsid protein and had no antiviral activity. PTX3 was expressed at high levels by myeloid cells in blood and lungs, and its plasma concentrations have strong and independent prognostic significance for death in individuals with COVID-19 (refs. ^{16,29}). It remains to be elucidated whether PTX3 plays a role in nucleocapsid-mediated complement activation and cytokine production^{30–32}.

MBL recognized the SARS-CoV-2 spike protein, including that of four VoC, and had antiviral activity in vitro against all of them, including the B.1.617.2 variant (Delta), which is currently a major concern worldwide. MBL has previously been shown to bind SARS-CoV spike protein³³. The interaction of MBL with SARS-CoV-2 spike protein required a trimeric conformation of the viral protein, did not involve direct recognition of the RBD and was glycan dependent, as expected. Site-specific glycosylation analysis of the SARS-CoV-2 spike protein revealed the presence of various oligomannose-type glycans across the protein¹⁸.

Molecular modeling reported here suggests that the MBL trimer interacts with glycans attached to the residues N603, N801 and N1074 on the same chain or N603, N709 and N1074 with N709 on a different chain. In both cases, the hypothesized MBL-binding site spans across the S1 and S2 regions of SARS-CoV-2 spike protein, suggesting a possible neutralization mechanism. The binding of MBL could prevent the detachment of the S1 region and the release of the fusion peptide at position 815, thus inhibiting virus entry into host cells. However, the mechanisms responsible for the antiviral activity of MBL remain to be fully defined. It is noteworthy that C-type lectins have been reported to act as entry receptors (or co-receptors)^{34–36}, and MBL is likely to compete at this level.

In apparent contrast with our results, ficolin-2 and collectin-11 were recently shown to interact with spike and nucleocapsid proteins, MBL with nucleocapsid protein and SP-D with spike protein^{37,38}. Experimental approaches used in these studies may explain the discrepancy with our results; whereas commercially available and in-house-produced recombinant pentraxins, C1q, MBL, ficolins, surfactant proteins and collectins were used in our study, serum was used as a source of PRMs by others³⁷, which may result in indirect interaction of MBL, ficolin-2 or collectin-11 with viral proteins mediated by a serum component. For instance, MASP-2

Fig. 5 | Inhibition by MBL of SARS-CoV-2 infection of primary respiratory cells. **a**, SARS-CoV-2 production at the HBEC apical surface at 72 h after infection in the presence of 10 or 50 $\mu\text{g ml}^{-1}$ (34 or 170 nM) MBL. Data are presented as mean values; $n=3$ independent experiments performed in triplicate (two donors) or single (one donor) cell cultures are shown. P values were determined by one-way ANOVA with Bonferroni's correction (**a**); $***P=2.85 \times 10^{-5}$ and $**P=0.0032$. **b–e**, Colocalization of SARS-CoV-2 spike protein and MBL in infected HBECs. **b**, Confocal analysis of the localization of SARS-CoV-2 spike protein (green) and MBL (red) in HBEC cultures infected with SARS-CoV-2 in the presence or absence of MBL (50 $\mu\text{g ml}^{-1}$; 170 nM); left, merged images of fluorescence signals; right, single extracted signals. Representative medium intensity projection (MIP) images of z stacks acquired in tiling modality are shown; $n=2$ cellular replicates per condition from one donor, four and nine z stacks; scale bar, 30 μm . **c**, Left, extracted signals of SARS-CoV-2 spike protein and MBL of **b**; scale bar, 30 μm ; right, colocalization rate between SARS-CoV-2 spike protein (S) and MBL (10 or 50 $\mu\text{g ml}^{-1}$; 34 or 170 nM). Each spot corresponds to a single xyz image presented as MIP. Data are presented as mean \pm s.e.m.; basal (-), $n=4$ z stacks; S, $n=4$ z stacks; S/MBL, 10, $n=8$ z stacks; S/MBL, 50, $n=12$ z stacks, from two cellular replicates. **d**, A 3D rendering of **b** (right), showing a blended reconstruction of the localization between SARS-CoV-2 spike protein and MBL in HBEC cultures; left, contribution of merged signals; scale bar, 30 μm ; middle, extracted image of signal from SARS-CoV-2 spike protein and MBL; right, close-up image that refers to the area outlined in white. A 3D rendering of a representative z stack of **c**. **e**, Stimulated emission depletion (STED) analysis of the localization of SARS-CoV-2 spike protein and MBL in HBECs; $N=1$ cell culture and seven STED acquisitions; left, merged signals of SARS-CoV-2 spike protein and MBL and the nucleus; right, single extracted signals; scale bar, 3 μm .

was shown to interact with nucleocapsid protein³⁷, confirming a previous study³⁰. MASPs are normally present in plasma complexed with molecules of the lectin pathway, thus explaining the

interactions of MBL with nucleocapsid protein, which was not observed in our study. Concerning SP-D, Hsieh et al. observed an interaction between a recombinant fragment of SP-D and spike

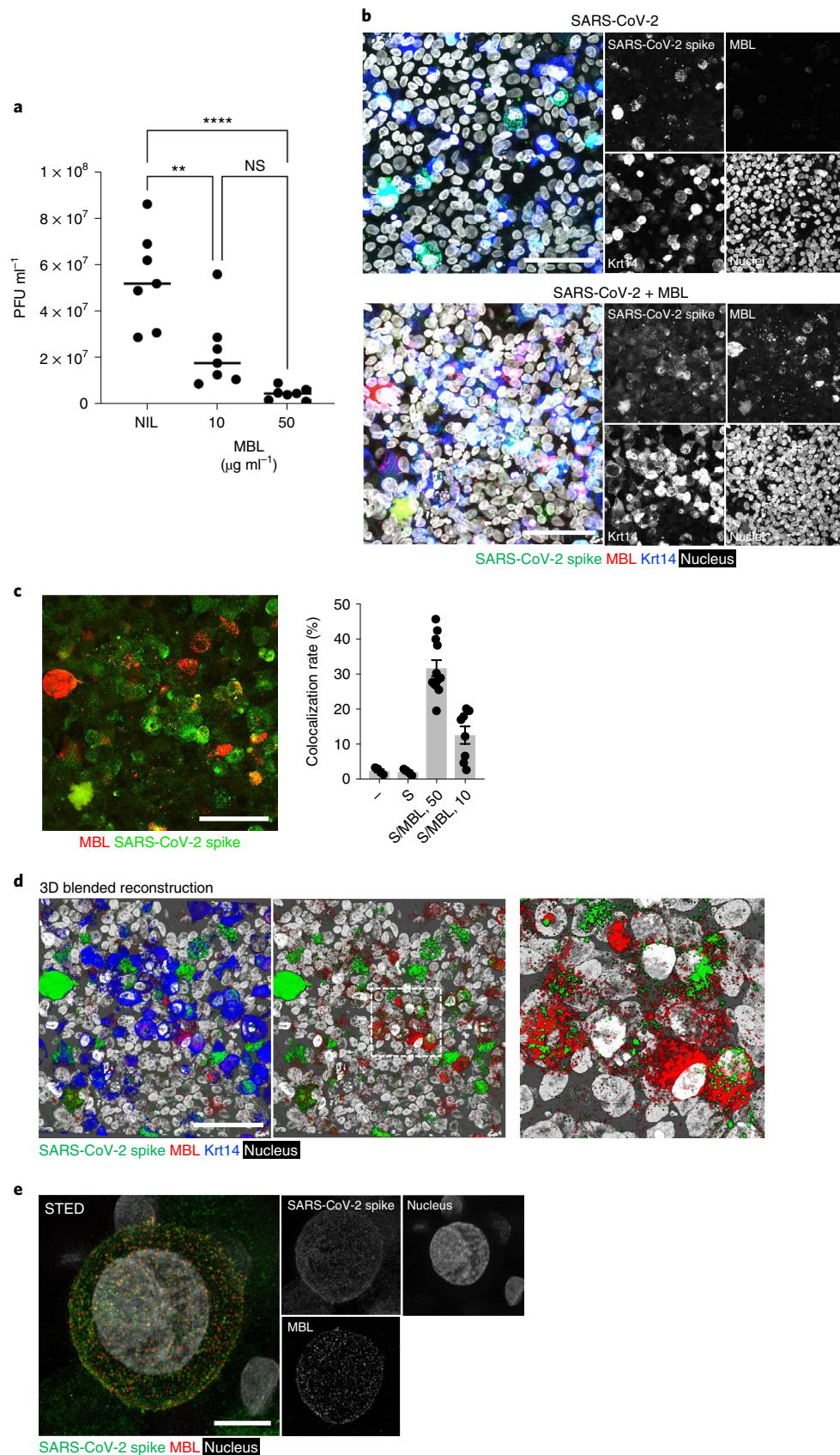


Table 1 | Association analysis results: candidate SNP association analysis

SNP	rsID	Variation	A1/A2 (legacy)	MAF infected	MAF healthy	OR	95% CI	<i>P</i> ^a	Direction (A1) ^b
chr10:52771466:C:T	rs1800451	p.Gly57Glu	T/C (C/A)	0.017	0.021	0.814	0.39–1.72	0.588	Lowers MBL levels
chr10:52771475:C:T	rs1800450	p.Gly54Asp	T/C (B/A)	0.017	0.15	1.070	0.83–1.39	0.609	Lowers MBL levels
chr10:52771482:G:A	rs5030737	p.Arg52Cys	A/G (D/A)	0.077	0.06	1.434	1.00–2.05	0.049	Lowers MBL levels
chr10:52771701:G:A	rs7095891	Promoter region	A/G	0.221	0.243	0.827	0.66–1.04	0.104	–
chr10:52771925:G:C	rs7096206	Promoter eQTL in liver (<i>P</i> = 1.7 × 10 ⁻¹⁷)	G/C (X/Y)	0.215	0.205	1.201	0.96–1.51	0.113	Lowers MBL levels
chr10:52772254:G:C	rs11003125	Promoter eQTL in liver (<i>P</i> = 9.1 × 10 ⁻⁶)	C/G	0.342	0.364	0.886	0.73–1.09	0.236	Increases MBL levels

The SNP column is in the format chromosome:position:reference allele:alternative allele. The position refers to the hg38 version of the genome. A1/A2 refers to minor/major alleles; legacy names refer to allele names as indicated in the literature (see text for relevant references); A, wild-type allele; B, C and D, alternative alleles, collectively called 'allele O'; Y and X, wild-type and alternative alleles of the rs7096206 polymorphism. MAF, minor allele frequency; rsID, reference sequence identification number; eQTL, expression quantitative trait loci. ^a Bonferroni threshold for significance is *P* < 0.008. ^b Direction derived from either the literature or the Genotype-Tissue Expression (GTEx) database (<https://www.gtexportal.org/home/>).

Table 2 | Locus-wide association analysis

SNP	rsID	A1	MAF infected	MAF healthy	OR	95% CI	<i>P</i> ^a
chr10:53229424:C:T	rs150342746	T	0.026	0.008	3.474	1.808–6.676	1.86 × 10 ⁻⁴
chr10:52963964:G:A	rs10824845	A	0.124	0.072	1.762	1.297–2.393	2.91 × 10 ⁻⁴
chr10:53083059:C:A	rs11816263	A	0.386	0.315	1.422	1.173–1.725	3.47 × 10 ⁻⁴
chr10:53104393:A:G	rs74974397	G	0.071	0.041	1.813	1.235–2.661	0.0024
chr10:53082503:A:AT	rs71032688	A	0.258	0.191	1.415	1.128–1.776	0.0025
chr10:53155596:C:T	rs117108247	T	0.069	0.042	1.750	1.195–2.561	0.0040

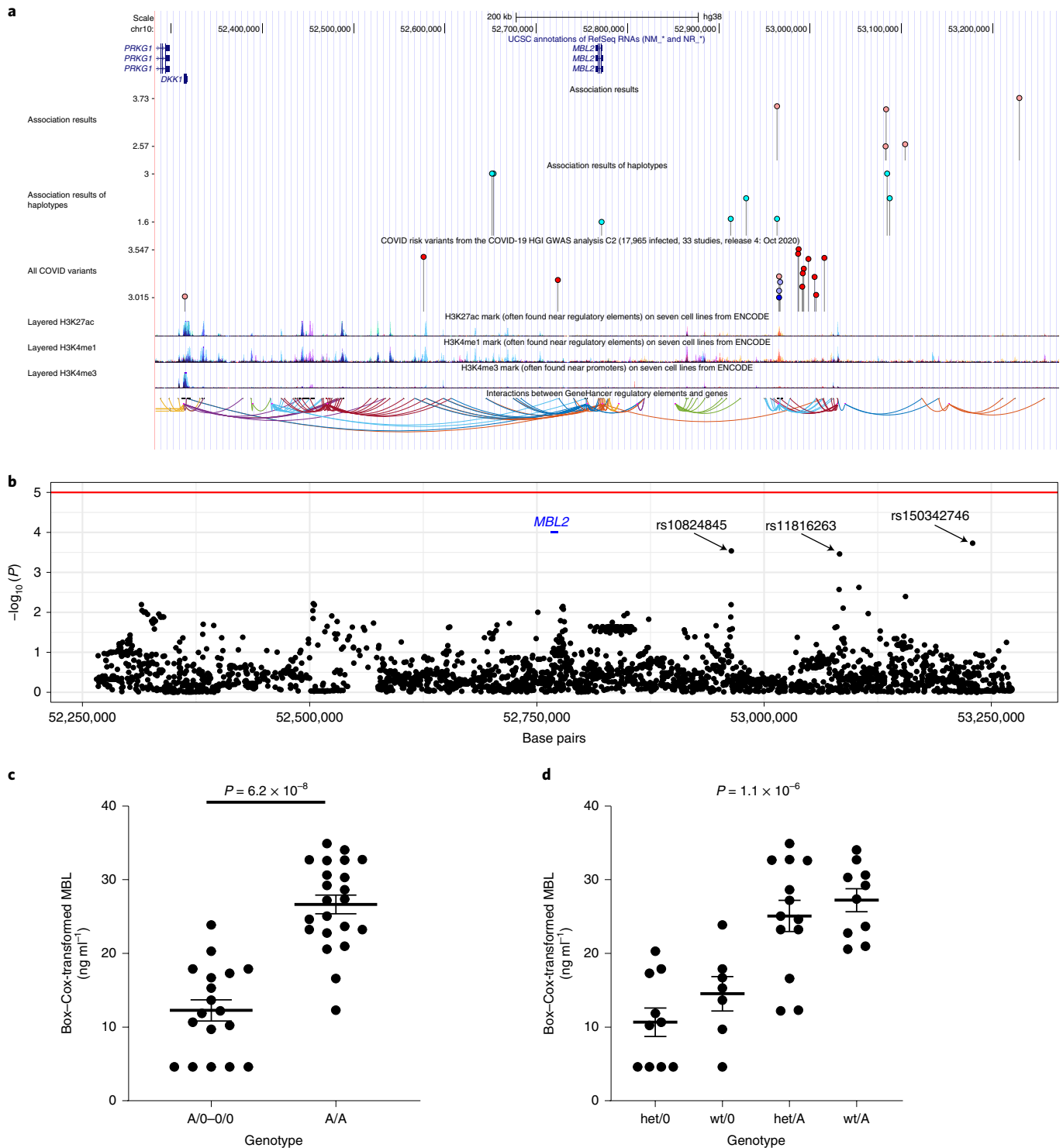
The SNP column is in the format chromosome:position:reference allele:alternative allele. The position refers to the hg38 version of the genome. SNPs with a *P* value of <0.0050 are shown. ^a Bonferroni threshold for significance is *P* < 1.5 × 10⁻⁵.

protein, whereas the recombinant full-length molecule showed a very low affinity for spike protein³⁸. To strengthen our results, we repeated the binding experiments using four different preparations of recombinant ficolin-2, two of SP-D and two of collectin-11 (as a single molecule or as collectin-10/collectin-11 heterocomplexes)³⁹, and we did not observe interaction with viral proteins. The studies by Ali et al.³⁷ and Hsieh et al.³⁸ have the merit to underline the involvement of the lectin pathway in SARS-CoV-2-dependent complement activation. Here, we provide a rigorous, solid, reliable and comprehensive picture of recognition of SARS-CoV-2 components by 'ante-antibodies'.

Interestingly, the *in silico* analysis presented here indicates that mutations in variants reported until now, including Omicron, do not affect glycosylation sites containing oligomannose-type glycans potentially recognized by MBL. In addition, binding and infection experiments show that the antiviral activity of MBL is not affected by these mutations. This finding indicates that the glycosylation sites are generally spared by selective pressure, suggesting that they are essential for SARS-CoV-2 infectivity. It has been recently shown that mechanisms of *in vitro* escape of SARS-CoV-2 from highly neutralizing COVID-19 convalescent plasma include the insertion of a new glycan sequon in the N-terminal domain of the spike protein, which leads to complete resistance to neutralization⁴⁰. This result further emphasizes the relevance of spike glycosidic moieties targeted by MBL in SARS-CoV-2 infectivity.

MBL was found to interact with spike protein and have antiviral activity with an EC₅₀ of approximately 0.08 μg ml⁻¹ (0.27 nM) and an

affinity of 34 nM. These concentrations are well in the range of those found in the blood of healthy individuals (up to 10 μg ml⁻¹), which increase two- to threefold during the acute-phase response. MBL plasma concentrations in healthy individuals are extremely variable, in part depending on genetic variation in the *MBL2* gene²¹. Defective MBL production has been associated with an increased risk of infections, in particular in primary or secondary immunodeficient children⁴¹. In SARS, conflicting results have been reported concerning the relevance of *MBL2* genetic variants in this condition^{22,42,43}. In COVID-19, one *MBL2* polymorphism has been associated with the development and severity of infection⁴⁴. We investigated the possible role of *MBL2* genetic variants in determining susceptibility to severe COVID-19 with respiratory failure. Surprisingly, and in contrast with a previous study⁴⁴, we found only a borderline correlation between one haplotype of the six SNPs associated with MBL levels and frequency of severe COVID-19 cases. However, we found a significant predisposing effect in individuals carrying *MBL2* biallelic functional variants and a total of seven significantly associated haplotypes, distributed along the *MBL2* genomic region, often mapping in correspondence of regulatory elements (such as enhancers, promoter regions and histone marks). Our association data are reinforced by the meta-analysis results obtained by integrating the summary statistics from a European cohort of >113,000 individuals and by the fact that one of our second best associations (rs10824845) maps in proximity of a cluster of suggestive signals identified by the COVID-19 HGI (<https://www.covid19hg.org/>), which includes data from up to 33 different worldwide studies. Further, the Regeneron



Genetic Center database²⁸ reports significant associations on rare and ultrarare variant analyses. Finally, the *rs5030737* (p.Arg52Cys) polymorphism in *MBL2* has been described in the UK Biobank International Classification of Diseases (ICD) PheWeb database (<https://pheweb.org/UKB-SAIGE/>) as a top signal in determining both 'dependence on respirator [Ventilator] or supplemental oxygen' (ICD code Z99.1; $P = 2.7 \times 10^{-4}$) and 'Respiratory failure, insufficiency, arrest' (ICD code J96; $P = 2.7 \times 10^{-3}$). These observations suggest that genetic variations in *MBL2*, possibly involved in the modulation of the expression of the gene in hepatocytes and,

interestingly, in macrophages, could play a role in determining susceptibility to severe COVID-19 with respiratory failure. Therefore, genetic analysis is consistent with the view that MBL recognition of SARS-CoV-2 plays an important role in COVID-19 pathogenesis.

Following interaction with spike protein, MBL was found to activate the lectin pathway of complement, as expected. Complement has been credited an important role in hyperinflammation underlying severe disease and is considered a relevant therapeutic target^{45,46}. Therefore, as for innate immunity in general including the IFN pathway⁴⁷, MBL-mediated recognition of SARS-CoV-2 may act

Fig. 6 | The MBL2 locus: structure and main association signals with severe COVID-19. **a**, A screenshot from the University of California Santa Cruz (UCSC) Genome browser (<http://genome.ucsc.edu/>; release December 2013, GRCh38/hg38) specifically highlighting the 1-Mb region surrounding the MBL2 gene is shown. Reported, in order, are the following tracks: (1) the ruler with the scale at the genomic level; (2) chromosome 10 (chr10) nucleotide numbering; (3) the UCSC RefSeq track; (4) COVID-19 risk variants from our study (lollipops show only signals at $P < 3 \times 10^{-3}$); (5) COVID-19 risk haplotypes, marked by the tagging SNP, from our study (lollipops show all haplotypes reported in Supplementary Tables 1 and 2); (6) COVID-19 risk variants from the COVID-19 Host Genetics Initiative (HGI) genome-wide association study (GWAS) analysis C2 (17,965 infected individuals, 33 studies, release 4, October 2020); (7) ENCODE data (<https://www.encodeproject.org/>) for H3K27ac, H3K4me1 and H3K4me3 histone modification marks, all derived from seven cell lines, and (8) the GeneHancer regulatory elements track; kb, kilobases. **b**, Manhattan plot of the single-SNP association analysis. The horizontal line represents the suggested $P = 5 \times 10^{-5}$ significance level. SNPs showing the lowest P value signals are indicated by an arrow; **rs150342746**: $P = 1.86 \times 10^{-4}$, OR = 3.474, 95% CI = 1.808–6.676; **rs10824845**: $P = 2.91 \times 10^{-4}$, OR = 1.762, 95% CI = 1.297–2.393; **rs11816263**: $P = 3.47 \times 10^{-4}$, OR = 1.422, 95% CI = 1.173–1.725. A logistic regression analysis was used. Bonferroni threshold for significance corresponds to $P < 1.5 \times 10^{-5}$. **c**, MBL plasma concentrations in individuals with COVID-19 carrying the wild-type allele (A/A) for the **rs1800451**, **rs1800450** and **rs5030737** SNPs compared to individuals carrying at least one copy of any alternative allele (O). Data are presented as mean \pm s.e.m.; $n = 17$ A/O- or O/O- and $n = 23$ A/A-carrying individuals. P value was analyzed by two-tailed t -test. **d**, MBL plasma concentrations in individuals with COVID-19 stratified based on the genotypes of the **rs10824845** (wild-type (wt) or heterozygous (het) in our cohort) and the presence of A or O alleles, as described for **c**. Box-Cox transformation was used to normalize the data. Data represent mean \pm s.e.m.; $n = 10$ O/het, $n = 7$ O/wt, $n = 13$ A/het and $n = 10$ A/wt individuals. P value was analyzed by ANOVA.

as a double-edged sword. In early phases of the disease, MBL may serve as a mechanism of antiviral resistance by blocking viral entry, whereas in advanced disease stages, it may contribute to complement activation and uncontrolled inflammation.

MBL has been safely administered to individuals with cystic fibrosis and chronic lung infections in which MBL deficiency contributes to pathogenesis^{48,49}. Therefore, the results presented here have translational implications both in terms of comprehensive genetic risk assessment and development of local or systemic therapeutic approaches.

Online content

Any methods, additional references, Nature Research reporting summaries, source data, extended data, supplementary information, acknowledgements, peer review information; details of author contributions and competing interests; and statements of data and code availability are available at <https://doi.org/10.1038/s41590-021-01114-w>.

Received: 21 June 2021; Accepted: 9 December 2021;
Published online: 31 January 2022

References

- Wu, F. et al. A new coronavirus associated with human respiratory disease in China. *Nature* **579**, 265–269 (2020).
- Zhu, N. et al. A novel coronavirus from patients with pneumonia in China, 2019. *N. Engl. J. Med.* **382**, 727–733 (2020).
- Hartenian, E. et al. The molecular virology of coronaviruses. *J. Biol. Chem.* **295**, 12910–12934 (2020).
- Wang, J., Jiang, M., Chen, X. & Montaner, L. J. Cytokine storm and leukocyte changes in mild versus severe SARS-CoV-2 infection: review of 3939 COVID-19 patients in China and emerging pathogenesis and therapy concepts. *J. Leukoc. Biol.* **108**, 17–41 (2020).
- Bottazzi, B., Doni, A., Garlanda, C. & Mantovani, A. An integrated view of humoral innate immunity: pentraxins as a paradigm. *Annu. Rev. Immunol.* **28**, 157–183 (2010).
- Holmskov, U., Thiel, S. & Jensenius, J. C. Collections and ficolins: humoral lectins of the innate immune defense. *Annu. Rev. Immunol.* **21**, 547–578 (2003).
- Garlanda, C., Bottazzi, B., Magrini, E., Inforzato, A. & Mantovani, A. PTX3, a humoral pattern recognition molecule, in innate immunity, tissue repair, and cancer. *Physiol. Rev.* **98**, 623–639 (2018).
- Reading, P. C. et al. Antiviral activity of the long chain pentraxin PTX3 against influenza viruses. *J. Immunol.* **180**, 3391–3398 (2008).
- Bozza, S. et al. Pentraxin 3 protects from MCMV infection and reactivation through TLR sensing pathways leading to IRF3 activation. *Blood* **108**, 3387–3396 (2006).
- Han, B. et al. Protective effects of long pentraxin PTX3 on lung injury in a severe acute respiratory syndrome model in mice. *Lab. Invest.* **92**, 1285–1296 (2012).
- Merad, M. & Martin, J. C. Pathological inflammation in patients with COVID-19: a key role for monocytes and macrophages. *Nat. Rev. Immunol.* **20**, 355–362 (2020).
- Severe Covid-19 GWAS Group et al. Genomewide association study of severe Covid-19 with respiratory failure. *N. Engl. J. Med.* **383**, 1522–1534 (2020).
- Zhang, Q. et al. Inborn errors of type I IFN immunity in patients with life-threatening COVID-19. *Science* **370**, eabd4570 (2020).
- Pairo-Castineira, E. et al. Genetic mechanisms of critical illness in COVID-19. *Nature* **591**, 92–98 (2021).
- Fajgenbaum, D. C. & June, C. H. Cytokine storm. *N. Engl. J. Med.* **383**, 2255–2273 (2020).
- Brunetta, E. et al. Macrophage expression and prognostic significance of the long pentraxin PTX3 in COVID-19. *Nat. Immunol.* **22**, 19–24 (2021).
- Zeng, W. et al. Biochemical characterization of SARS-CoV-2 nucleocapsid protein. *Biochem. Biophys. Res. Commun.* **527**, 618–623 (2020).
- Watanabe, Y., Allen, J. D., Wrapp, D., McLellan, J. S. & Crispin, M. Site-specific glycan analysis of the SARS-CoV-2 spike. *Science* **369**, 330–333 (2020).
- Chu, H. et al. Comparative tropism, replication kinetics, and cell damage profiling of SARS-CoV-2 and SARS-CoV with implications for clinical manifestations, transmissibility, and laboratory studies of COVID-19: an observational study. *Lancet Microbe* **1**, e14–e23 (2020).
- Desmyter, J., Melnick, J. L. & Rawls, W. E. Defectiveness of interferon production and of rubella virus interference in a line of African green monkey kidney cells (Vero). *J. Virol.* **2**, 955–961 (1968).
- Garred, P. et al. A journey through the lectin pathway of complement–MBL and beyond. *Immunol. Rev.* **274**, 74–97 (2016).
- Ip, W. K. et al. Mannose-binding lectin in severe acute respiratory syndrome coronavirus infection. *J. Infect. Dis.* **191**, 1697–1704 (2005).
- Lipscombe, R. J. et al. High frequencies in African and non-African populations of independent mutations in the mannose binding protein gene. *Hum. Mol. Genet.* **1**, 709–715 (1992).
- Sumiya, M. et al. Molecular basis of opsonic defect in immunodeficient children. *Lancet* **337**, 1569–1570 (1991).
- Madsen, H. O. et al. A new frequent allele is the missing link in the structural polymorphism of the human mannan-binding protein. *Immunogenetics* **40**, 37–44 (1994).
- Madsen, H. O. et al. Interplay between promoter and structural gene variants control basal serum level of mannan-binding protein. *J. Immunol.* **155**, 3013–3020 (1995).
- Fishilevich, S. et al. GeneHancer: genome-wide integration of enhancers and target genes in GeneCards. *Database* **2017**, bax028 (2017).
- Kosmicki, J. A. et al. A catalog of associations between rare coding variants and COVID-19 outcomes. Preprint at *medRxiv* <https://doi.org/10.1101/2020.10.28.20221804> (2021).
- Schirinzii, A. et al. Pentraxin 3: potential prognostic role in SARS-CoV-2 patients admitted to the emergency department. *J. Infect.* **82**, 84–123 (2021).
- Gao, T. et al. Highly pathogenic coronavirus N protein aggravates lung injury by MASP-2-mediated complement over-activation. Preprint at *medRxiv* <https://doi.org/10.1101/2020.11.03.1129.20041962> (2020).
- Karwaciak, I., Salkowska, A., Karas, K., Dastych, J. & Ratajowski, M. Nucleocapsid and spike proteins of the coronavirus SARS-CoV-2 induce IL6 in monocytes and macrophages-potential implications for cytokine storm syndrome. *Vaccines* **9**, 54 (2021).
- McBride, R., van Zyl, M. & Fielding, B. C. The coronavirus nucleocapsid is a multifunctional protein. *Viruses* **6**, 2991–3018 (2014).

33. Zhou, Y. et al. A single asparagine-linked glycosylation site of the severe acute respiratory syndrome coronavirus spike glycoprotein facilitates inhibition by mannose-binding lectin through multiple mechanisms. *J. Virol.* **84**, 8753–8764 (2010).
34. Lu, Q. et al. SARS-CoV-2 exacerbates proinflammatory responses in myeloid cells through C-type lectin receptors and Tweety family member 2. *Immunity* **54**, 1304–1319 (2021).
35. Lempp, F. A. et al. Lectins enhance SARS-CoV-2 infection and influence neutralizing antibodies. *Nature* **598**, 342–347 (2021).
36. Chiodo, F. et al. Novel ACE2-independent carbohydrate-binding of SARS-CoV-2 spike protein to host lectins and lung microbiota. Preprint at *bioRxiv* <https://doi.org/10.1101/2020.05.13.092478> (2020).
37. Ali, Y. M. et al. Lectin pathway mediates complement activation by SARS-CoV-2 proteins. *Front. Immunol.* **12**, 714511 (2021).
38. Hsieh, M. H. et al. Human surfactant protein D binds spike protein and acts as an entry inhibitor of SARS-CoV-2 pseudotyped viral particles. *Front. Immunol.* **12**, 641360 (2021).
39. Bayarri-Olmos, R. et al. Development of a quantitative assay for the characterization of human collectin-11 (CL-11, CL-K1). *Front. Immunol.* **9**, 2238 (2018).
40. Andreano, E. et al. SARS-CoV-2 escape in vitro from a highly neutralizing COVID-19 convalescent plasma. Preprint at *bioRxiv* <https://doi.org/10.1101/2020.12.28.424451> (2020).
41. Koch, A. et al. Acute respiratory tract infections and mannose-binding lectin insufficiency during early childhood. *JAMA* **285**, 1316–1321 (2001).
42. Zhang, H. et al. Association between mannose-binding lectin gene polymorphisms and susceptibility to severe acute respiratory syndrome coronavirus infection. *J. Infect. Dis.* **192**, 1355–1361 (2005).
43. Yuan, F. F. et al. Influence of *FcγRIIA* and *MBL* polymorphisms on severe acute respiratory syndrome. *Tissue Antigens* **66**, 291–296 (2005).
44. Medetalibeyoglu, A. et al. Mannose binding lectin gene 2 (rs1800450) missense variant may contribute to development and severity of COVID-19 infection. *Infect. Genet. Evol.* **89**, 104717 (2021).
45. Risitano, A. M. et al. Complement as a target in COVID-19? *Nat. Rev. Immunol.* **20**, 343–344 (2020).
46. Carvelli, J. et al. Association of COVID-19 inflammation with activation of the C5a–C5aR1 axis. *Nature* **588**, 146–150 (2020).
47. King, C. & Sprent, J. Dual nature of type I interferons in SARS-CoV-2-induced inflammation. *Trends Immunol.* **42**, 312–322 (2021).
48. Garred, P. et al. Mannose-binding lectin (MBL) therapy in an MBL-deficient patient with severe cystic fibrosis lung disease. *Pediatr. Pulmonol.* **33**, 201–207 (2002).
49. Jensenius, J. C., Jensen, P. H., McGuire, K., Larsen, J. L. & Thiel, S. Recombinant mannan-binding lectin (MBL) for therapy. *Biochem. Soc. Trans.* **31**, 763–767 (2003).

Publisher's note Springer Nature remains neutral with regard to jurisdictional claims in published maps and institutional affiliations.

© The Author(s), under exclusive licence to Springer Nature America, Inc. 2022

Methods

Participant cohorts and ethical approvals. Approvals were obtained from the relevant ethics committees (Humanitas Clinical and Research Center, reference number, 316/20; the University of Milano-Bicocca School of Medicine, San Gerardo Hospital, reference number, 84/2020). The requirement for informed consent was waived.

For genetic association analyses, we investigated 2,000 individuals. This population included 332 individuals with severe COVID-19, defined as hospitalization with respiratory failure and a confirmed SARS-CoV-2 viral RNA PCR test from nasopharyngeal swabs. Individuals were recruited from intensive care units and general wards at two hospitals in the Milan area (Humanitas Clinical and Research Center, IRCCS, Rozzano, Italy (140 individuals); San Gerardo Hospital, Monza, Italy (192 individuals)). Additionally, 1,668 healthy individuals from the general Italian population with unknown COVID-19 status were investigated.

MBL plasma concentrations were analyzed in a cohort of 40 individuals, including all males and non-pregnant females, 18 years of age or older and admitted to Humanitas Clinical and Research Center (Rozzano, Milan, Italy) between March and April 2020 with a laboratory-confirmed diagnosis of COVID-19.

Recombinant proteins and antibodies. Recombinant SARS-CoV-2 proteins used are listed in Supplementary Table 6. Recombinant human PTX3 and its domains were produced in-house, as described in ref.⁵⁰. Recombinant human SP-A was from Origene. Recombinant human MBL, collectin-12, ficolin-1, ficolin-2 and ficolin-3 were from Biotechne. Other recombinant preparations of ficolin-2 were from Abnova, Origene and SinoBiological. SP-D was from Biotechne and SinoBiological. Recombinant human collectin-10 and collectin-11 were from Abnova. Recombinant human collectin-11 or collectin-10/collectin-11 heterocomplexes were also expressed and purified, as described in ref.³⁹. Purified human C1q was from Complement Technology, purified CRP was from Millipore, and purified SAP was from Abcam. Rabbit anti-PTX3 (1:5,000) was produced in-house⁵⁰, and rabbit anti-MBL (1:5,000) was from Abcam. Polyclonal anti-C1q (1:5,000) was from Dako. Anti-CRP (1:5,000) and anti-SAP (1:5,000) were from Merck. Mouse monoclonal IgG anti-human collectin-11 (clone Hyb-15, 1:2,000) and mouse monoclonal IgG anti-human ficolin-2 (clone FCN219) were produced in-house^{39,51}. The following secondary antibodies were used: HRP-linked donkey anti-rabbit IgG (GE Healthcare, 1:5,000) and HRP-linked sheep anti-mouse IgG (GE Healthcare, 1:5,000).

Binding of humoral PRMs to SARS-CoV-2 proteins. Recombinant His tag SARS-CoV-2 proteins were immobilized (concentrations ranging from 6.25 to 50 pmol ml⁻¹) on 96-well nickel-coated plates (Thermo Fisher Scientific) for 1 h at 20 °C. Plates were then blocked for 2 h at 37 °C with 200 µl of 2% bovine serum albumin (BSA) in 10 mM Tris-HCl buffer, pH 7.5, containing 150 mM NaCl, 2 mM CaCl₂ and 0.1% Tween 20 (TBST-Ca²⁺). Plates were washed three times with TBST-Ca²⁺ and incubated for 1 h at 37 °C with 100 µl of PTX3 (4 µg ml⁻¹ (12 nM) in TBST-Ca²⁺), MBL (1–2 µg ml⁻¹ (3.4–6.7 nM) in TBST-Ca²⁺), C1q (4 µg ml⁻¹ (10 nM) in TBST-Ca²⁺), CRP (3 µg ml⁻¹ (25 nM) in TBST-Ca²⁺) and SAP (4 µg ml⁻¹ (32 nM) in TBST-Ca²⁺), ficolin-2 (1 µg ml⁻¹ (2.5 nM) in TBST-Ca²⁺), collectin-11 (1 µg ml⁻¹ (6.7 nM) in TBST-Ca²⁺). After washes, plates were incubated for 1 h at 37 °C with specific primary antibodies, followed by HRP-conjugated secondary antibodies diluted in TBST-Ca²⁺ buffer. After development with the chromogenic substrate 3,3',5,5'-tetramethylbenzidine (TMB; Thermo Fisher Scientific), binding was detected by absorbance at 450 nm on a Spectrostar Nano Microplate Reader (BMG Labtech). Values from blank wells were subtracted from those recorded from sample wells.

For binding experiments of SARS-CoV-2 spike protein to collectin-10/collectin-11 heterocomplexes, spike protein was immobilized on a 96-well Nunc Maxisorp plate. MBL (1 µg ml⁻¹; 3.4 nM) or collectin-10/collectin-11 heterocomplexes (1 µg ml⁻¹; 3.4 nM) in TBST-Ca²⁺ were then incubated for 1 h at 37 °C, followed by incubation with specific primary antibodies³⁹, HRP-conjugated secondary antibodies and TMB development.

In other experiments, 100 µl of 2 µg ml⁻¹ rhMBL (6.7 nM), collectin-12 (6.7 nM), ficolin-1 (5 nM), ficolin-2 (5 nM) and ficolin-3 (3 nM) and SP-A (3 nM) or SP-D (3.4 nM) in PBS were immobilized on 96-well Nunc Maxisorp Immunoplates (Costar) overnight at 4 °C. Plates were blocked with 200 µl of 2% BSA-TBST-Ca²⁺ for 2 h at 37 °C. Biotinylated SARS-CoV-2 spike protein was added for 1 h at 37 °C, followed by the addition of HRP-conjugated streptavidin (1:10,000, Biospa) for 1 h at 37 °C and TMB development.

For competition-based experiments, biotinylated SARS-CoV-2 spike protein was captured on 96-well neutravidin-coated plates for 1 h at 37 °C. Plates were incubated for 1 h at 37 °C with 100 µl of rhMBL (0.25 µg ml⁻¹; 0.83 nM) alone or in the presence of D-mannose, N-acetyl-glucosamine or D-glucose (Sigma-Aldrich). Bound MBL was detected by incubation with rabbit anti-MBL, followed by HRP-conjugated secondary antibody and TMB development.

For PTX3/SARS-CoV-2 nucleocapsid interaction studies, PTX3 and its recombinant domains were immobilized on a 96-well Nunc Maxisorp plate. Biotinylated SARS-CoV-2 nucleocapsid protein was then added for 1 h at 37 °C, followed by addition of HRP-conjugated streptavidin.

SPR studies. SPR analyses were performed at 25 °C on a Biacore 8K instrument (GE Healthcare). MBL was immobilized on the surface of a CM5 sensor chip through standard amine coupling. Briefly, after activation of the surface with a mixture of 1-ethyl-3-(3-dimethylaminopropyl) carbodiimide hydrochloride and N-hydroxysuccinimide, MBL was diluted at 50 nM in 10 mM sodium acetate buffer, pH 4.5, and injected over the surface (flow rate of 10 µl min⁻¹). Free activated sites were blocked by flowing 1 M ethanolamine, pH 8.5. Final MBL immobilization levels were around 4,500 RU (with 1 RU = 1 pg mm⁻²). A second surface was prepared without any ligand and used as a reference. Recombinant RBD and trimeric spike protein were produced in Expi293 cells and purified as reported in ref.⁵². Increasing concentrations of SARS-CoV-2 RBD or spike protein (2.5, 7.4, 22, 67, 200 and 600 nM) were injected using a single-cycle kinetics setting (flow rate of 30 µl min⁻¹); dissociation was followed for 10 mins. The running buffer was 10 mM Tris-buffered saline, pH 7.4, containing 150 mM NaCl, 2 mM CaCl₂ and 0.005% Tween 20. The interaction was also analyzed using the running buffer without CaCl₂. Analyte responses were corrected for non-specific binding and buffer responses through the use of reference channels. Binding kinetics were determined by fitting of the experimental curves with the Langmuir 1:1 model according to standard procedures; data analyses were performed with Biacore Insight Evaluation Software v2.0.15.12933. In the presence of CaCl₂, trimeric spike protein bound to MBL with a K_d (1/ms) of 2.1 × 10⁴, a K_d (1/s) of 7.3 × 10⁻⁴ and a K_D of 34 nM.

Computational modeling of the MBL-SARS-CoV-2 spike interaction. The model of the MBL trimer (UniProt⁵³ P11226) was created starting from the crystal structure of human mannose-binding protein⁵⁴ (Protein Data Bank (PDB): 1HUP). The N terminus of MBL was modeled as collagen based on the template crystal structure of the collagen triple helix model⁵⁵ (PDB: 1K6F). The binding site of mannose molecules was determined by aligning the MBL structure to the crystal structure of rat mannose protein A⁵⁶ (PDB: 1KX1). Reference distances (~40 Å) between mannose molecules were computed in PYMOL.

Putative binding sites of MBL were determined identifying all triplets of N-glycosylation sites at a distance between 35 Å and 50 Å in the closed-state SARS-CoV-2 spike protein⁵⁷. Distances were computed using the program ALMOST⁵⁸.

Pseudotyped virus production. Human 293T cells were transfected with a lentiviral vector expressing GFP under the control of a human phosphoglycerate kinase (PGK)⁵⁹ promoter and a pCMV-expressing vector containing the SARS-CoV-2 spike sequence (accession number MN908947) that was codon optimized for human expression and contained a deletion at the 3' end aimed at deleting 19 amino acid residues at the C terminus. An HIV gag-pol packaging construct and a rev-encoding plasmid were cotransfected by calcium phosphate for the production of infectious viral particles. Sixteen hours after transfection, the medium was replaced, and 30 h later, supernatant was collected and filtered through a 0.22-µm pore nitrocellulose filter. Viral particles were pelleted by ultracentrifugation. As a control, lentivirus particles were pseudotyped with the VSV-g glycoprotein that allows a high efficiency infection independently of binding to ACE2.

Pseudotyped lentivirus binding assay. Nunc Maxisorp Immunoplates (96-well, Costar) were coated with 100 µl of rhMBL (3 and 1 µg ml⁻¹; 10 and 3.4 nM in PBS). After overnight incubation, plates were blocked with 2% BSA in TBST-Ca²⁺ for 1 h at 37 °C, washed and incubated for 1 h with 100 µl of SARS-CoV-2 spike protein-pseudotyped lentivirus or VSV-pseudotyped lentivirus (from 0.1 to 1 µg ml⁻¹ in TBST-Ca²⁺). After washing, bound pseudotyped virus particles were lysed with 0.5% Triton X-100, and HIV p24 core protein was detected by ELISA (PerkinElmer).

Complement deposition assay. One hundred microliters of SARS-CoV-2 spike protein (either active trimer or non-covalent trimer; 1 µg ml⁻¹ in PBS) was captured on 96-well plates overnight at 4 °C. After washing, wells were incubated for 1 h at 37 °C with 10% normal human serum (ComplementTech), 10% C1q-depleted serum or 10% C4-depleted serum reconstituted or not with 25 µg ml⁻¹ purified C4 (Calbiochem); 10% heat-inactivated human serum (30 min at 56 °C) and 10% C3-depleted serum were used as negative controls. Sera were diluted in 10 mM Tris-buffered saline containing 0.5 mM MgCl₂, 2 mM CaCl₂ and 0.05% Tween 20, which was also used as washing buffer. For MBL immunodepletion, 10% normal human serum was incubated overnight with 0.6 µg ml⁻¹ rabbit anti-MBL. Bound MBL-antibody complexes were separated by Dynabeads Protein G (Thermo Fisher Scientific), and the supernatant (termed MBL-ID) was used in the assay (final concentration of 10%). C5b-9 deposition was assayed by incubation for 1 h at 37 °C with rabbit anti-sC5b-9 (ComplementTech) diluted 1:2,000 in washing buffer⁶⁰, followed by incubation with specific HRP-conjugated secondary antibodies and TMB development.

Cell lines. Vero and Vero E6 cell lines were obtained from the Istituto Zooprofilattico di Brescia, Italy, and ATCC, respectively, and maintained in Eagle's minimum essential medium (EMEM; Lonza) with 10% fetal bovine serum (FBS; Euroclone) and penicillin-streptomycin (complete medium).

Human embryonic kidney 293T cells containing the mutant gene of SV40 large T antigen (ATCC, CRL-3216) were cultured as described in ref. ⁶¹.

The human lung epithelial Calu-3 cell line was obtained from NovusPharma and grown in EMEM supplemented with 20% FBS and penicillin–streptomycin (complete medium).

HBECs. Isolation, culture and differentiation of primary HBECs were performed as reported in ref. ⁶². In brief, cells were obtained from mainstem human bronchi derived from three individuals undergoing lung transplant (BE37, BE63 and BE177). Epithelial cells were detached by overnight treatment of bronchi with protease XIV and were cultured in a serum-free medium (LHC9 mixed with RPMI 1640; 1:1) containing supplements⁶². Collection of bronchial epithelial cells was approved by the Ethics Committee of the Istituto Giannina Gaslini following Italian Ministry of Health guidelines (registration number ANTECER, 042-09/07/2018). Participants provided informed consent to the study.

To obtain differentiated epithelia, cells were seeded at high density (5×10^5 cells per snapwell) on 12-mm-diameter porous membranes (Snapwell inserts, Corning, 3801). After 24 h, the serum-free medium was removed from both sides and, on the basolateral side only, replaced with Pneumacult ALI medium (StemCell Technologies), and differentiation of cells (for 3 weeks) was performed under air–liquid interface (ALI) conditions.

Entry assay with SARS-CoV-2 spike-pseudotyped lentivirus particles.

293T cells were engineered to overexpress the SARS-CoV-2 entry receptor by transduction of a lentiviral vector expressing ACE2 (provided by M. Pizzato, University of Trento). The entry assay was optimized in 96-well plates by seeding 5×10^4 ACE2-overexpressing 293T cells per well; 24 h later, cells and SARS-CoV-2 spike-pseudotyped lentivirus stock (1:500) were incubated with serial dilutions of soluble PRM for 30 min. The SARS-CoV-2 spike-pseudotyped lentivirus was added to the cells, and 48 h later, cells were detached with accutase, fixed and analyzed for GFP expression by cytofluorimetry.

SARS-CoV-2 viral isolates. Viral isolation from clinical samples and use for research purposes was approved by the San Raffaele Hospital Institutional Review Board within the COVID-19 Biobanking project ‘COVID-Biob’ (34/int/2020 19 March 2020; ClinicalTrials.gov Identifier: NCT04318366). Each individual provided informed consent.

The following SARS-CoV-2 isolates were obtained from nasopharyngeal swabs: (1) B.1 lineage with the spike D614G mutation (GISAID accession ID: EPI_ISL_413489) from a mildly symptomatic individual by inoculation of Vero E6 cells^{63,64}, (2) South African B.1.351 (Beta) lineage (GISAID accession ID: EPI_ISL_1599180) from an Italian 80-year-old male individual, (3) B.1.1.7 (Alpha) lineage (GISAID accession ID: EPI_ISL_1924880) from an Italian 58-year-old female individual, (4) P.1 (Gamma) lineage (GISAID accession ID: EPI_ISL_1925323) from an Italian 43-year-old female individual and (5) B.1.617.2 (Delta) lineage (GISAID accession ID: EPI_ISL_4198505) from an Italian 50-year-old male individual. Secondary viral stocks were generated by infection of Vero E6 cells. Stocks were maintained at -80°C and titered by a plaque-forming assay.

Infections. Calu-3 cells were seeded in 48-well plates (Corning) at a concentration of 5×10^4 cells per well in complete medium 24 h before infection. Tenfold serial dilutions of MBL (from 0.01 to $10 \mu\text{g ml}^{-1}$; 0.034–34 nM) were incubated for 1 h with aliquots of SARS-CoV-2-containing supernatant to obtain an MOI of either 0.1 or 1 before incubation with Calu-3 cells (virus + MBL). Virus incubation with MBL was also combined with incubation of target cells. Briefly, both virus and Calu-3 cells were incubated with tenfold serial dilutions of MBL (from 0.01 to $10 \mu\text{g ml}^{-1}$; 0.034–34 nM). After 1 h, virus suspensions incubated with serial dilutions of MBL were added to MBL-treated cells (virus + cells + MBL). In both cases, 48 and 72 h after infection, cell culture supernatants were collected and stored at -80°C until determination of viral titers.

Forty-eight hours before infection, the apical surface of HBECs was washed with 500 μl of HBSS for 1.5 h at 37°C , and the cultures were moved into fresh ALI medium. Immediately before infection, apical surfaces were washed twice to remove accumulated mucus with 500 μl of HBSS for 30 min at 37°C . PTX3 or MBL was added to the apical surface for 1 h before the addition of 100 μl of viral inoculum at an MOI of 1. HBECs were incubated for 2 h at 37°C . Viral inoculum was then removed, and the apical surface of the cultures was washed three times with 500 μl of PBS. Cultures were incubated at 37°C for 72 h after infection. Infectious virus produced by HBECs was collected by washing the apical surface of the culture with 100 μl of PBS every 24 h up to 72 h after infection. Apical washes were stored at -80°C until analysis and titered by plaque assay. At 72 h after infection, cells were fixed in 4% paraformaldehyde for immunofluorescence analysis.

All infection experiments were performed in a BSL-3 laboratory (Laboratory of Medical Microbiology and Virology, Vita-Salute San Raffaele University).

Measurements were taken from distinct samples.

Plaque-forming assay. The viral stock titer was measured by a plaque-forming assay in Vero cells. Briefly, confluent Vero cells (1.5×10^6 cells per well) seeded

in six-well plates (Corning) were incubated in duplicate with 1 ml of EMEM with 1% FBS containing tenfold serial dilutions of SARS-CoV-2 stock. After 1 h, the viral inoculum was removed, and methylcellulose (Sigma; 1 ml in EMEM with 5% FBS) was overlaid on each well. After 4 d, cells were stained with 1% crystal violet (Sigma) in 70% methanol. Plaques were counted with a stereoscopic microscope (SMZ-1500, Nikon Instruments), and the virus titer was calculated as PFU per milliliter.

To determine the viral titers of the supernatant collected from Calu-3 cells and HBECs, confluent Vero cells (2.5×10^5 cells per well) were seeded in 24-well plates (Corning) 24 h before infection. Cells were then incubated with 300 μl of EMEM with 1% FBS containing serially diluted (1:10) virus-containing supernatants. The plaque-forming assay was performed as described above.

Chemokine quantification. Half of the ALI medium (1 ml) was collected from each well of the lower chamber every 24 h after infection and replaced with fresh ALI medium. The collected medium was stored at -80°C until analysis. Before chemokine quantification, 250 μl of medium was treated with 27 μl of Triton X-100 and heated for 30 min at 56°C to inactivate SARS-CoV-2 infectivity.

Chemokines (IL-8 and CXCL5) were quantified by ELISA (Quantikine ELISA kits, DY208 and DY254, R&D Systems).

Confocal and STED super-resolution microscopy. After 4% paraformaldehyde fixation, HBEC cultures were incubated for 1 h with PBS and 0.1% Triton X-100 (Sigma-Aldrich), 5% normal donkey serum (Sigma-Aldrich), 2% BSA and 0.05% Tween (blocking buffer). Cells were then incubated for 2 h in blocking buffer with the following primary antibodies: mouse anti-cytokeratin 14 (Krt14; LL002; $1 \mu\text{g ml}^{-1}$; 33-168, ProSci-Incorporated), rabbit polyclonal anti-spike protein (944-1218 amino acids; $2 \mu\text{g ml}^{-1}$; 28867-1-AP, Proteintech), rat anti-MBL (8G6; $1 \mu\text{g ml}^{-1}$; HM1035, Hycult Biotech) and rat anti-MBL (14D12; $1 \mu\text{g ml}^{-1}$; HM1038, Hycult Biotech). After washing with PBS and 0.05% Tween, cells were incubated for 1 h with the following species-specific cross-adsorbed secondary antibodies from Invitrogen-Thermo Fisher Scientific: donkey anti-rabbit IgG Alexa Fluor 488 ($1 \mu\text{g ml}^{-1}$; A-21206), donkey anti-rat IgG Alexa Fluor 594 ($1 \mu\text{g ml}^{-1}$; A-21209) and donkey anti-mouse IgG Alexa Fluor 647 ($1 \mu\text{g ml}^{-1}$; A-31571). DAPI (Invitrogen) was used for nucleus staining. Cells were mounted with Mowiol (Sigma-Aldrich) and analyzed with a Leica SP8 STED3X confocal microscope system equipped with a Leica HC PL APO CS2 $\times 63/1.40$ -NA oil immersion lens. Confocal images (1.024×1.024 pixels) were acquired in xyz and tiling modality (0.25- μm slice thickness) and at 1 Airy unit of lateral resolution (pinhole aperture of 95.5 μm) at a frequency of 600 Hz in bidirectional mode. Alexa Fluor 488 was excited with a 488-nm argon laser, and emission was collected from 505 to 550 nm. Alexa Fluor 594 was excited with a 594/604-nm tuned white light laser, and emission was collected from 580 to 620 nm. Alexa Fluor 647 was excited with a 640/648-nm tuned white light laser, and emission was collected from 670 to 750 nm. Frame sequential acquisition was applied to avoid fluorescence overlap. A gating between 0.4 and 7 ns was applied to avoid collection of reflection and autofluorescence. 3D STED analysis was performed using the same acquisition setup. A 660-nm CW-depletion laser (30% of power) was used for excitations of Alexa Fluor 488 (spike signal) and Alexa Fluor 594 (MBL signal). STED images were acquired with a Leica HC PL APO $\times 100/1.40$ -NA oil STED white objective at 572.3 milli-absorption unit. CW-STED and gated CW-STED were applied to Alexa Fluor 488 and Alexa Fluor 594, respectively. Confocal images were processed, 3D rendered and analyzed as colocalization rate between spike protein and MBL with Leica Application Suite X software (LASX, version 3.5.5.19976) and presented as MIP. STED images were deconvolved with Huygens Professional software (Scientific Volume Imaging B. V., version 19.10) and presented as MIP.

Genetic analysis and imputation. Details on DNA extraction, array genotyping and quality checks are reported elsewhere^{12,65}. Genetic coverage was increased by performing SNP imputation on the genome build GRCh38 using the Michigan Imputation Server (<https://imputation.biodatacatalyst.nhlbi.nih.gov/index.html#!>), and haplotypes were generated by the Trans-Omics for Precision Medicine (TOPMed) program (freeze 5)⁶⁶ for infected and healthy individuals. We used the population panel ‘ALL’ and filtered by an imputation of $R^2 > 0.1$. Next, we only retained SNPs with $R^2 \geq 0.6$ and $\text{MAF} \geq 1\%$. We then checked infected and healthy individuals for solving within-Italian relationships and for testing the possible existence of population stratification within and across batches by performing a principal-component analysis (PCA) using an linkage disequilibrium (LD)-pruned subset of SNPs across chromosome 10 and the Plink v.1.9 package⁶⁷. The final set of analyzed variants was composed of 3,425 SNPs distributed in the *MBL2* region (gene ± 500 kb).

MBL plasma concentration. Venous blood samples were collected during the first days after hospital admission (median (interquartile range): 3 (1–6) d), and EDTA plasma was stored at -80°C . MBL plasma concentrations were measured by ELISA (Hycult Biotech, HK323-02, detection limit of 0.41 ng ml^{-1}) by personnel blind to participant characteristics. Measurements were taken from distinct samples tested in duplicate. In each analytical session, a sample from a pool of healthy donor plasma was used as internal control.

Statistical analysis. Prism GraphPad software v. 8.0 (www.graphpad.com) was used for the statistical analyses. Comparisons among groups were performed using one or two-way ANOVA and a Bonferroni correction. Non-linear fit of transformed data was determined by using the log (agonist) versus response (three or four parameters). ROUT test or Rosner's test was applied to identify outliers. No outliers were identified, and all data were included in the statistical analyses used for Figs. 1–5 and Extended Data Figs. 1, 2 and 4. For Fig. 6c,d, three outliers were excluded based on Rosner's test.

For genetic studies, case–control allele–dose association tests were performed using the PLINK v.1.9 logistic regression framework for dosage data. Age, sex, age × age, sex × age and the first ten principal components from the PCA were introduced in the model as covariates. Analyses were conducted always referring to the minor allele. All *P* values are presented as not corrected and are accompanied by ORs and 95% CI values; however, in the relevant tables/figures, Bonferroni-corrected thresholds for significance are indicated in the footnote/legend.

In the genotyping analysis, we evaluated the distribution of infected and healthy individuals carrying functional SNPs (rs5030737, rs1800450, rs1800451 and rs7096206)^{23–26} in biallelic conditions. Rs5030737, rs1800450 and rs1800451 are located in the coding region of the gene, and they are known to result in severe impairment of the assembly of MBL trimeric structure. Alternative alleles of these SNPs are classically referred to as 'D', 'B' and 'C'; but usually the presence of either of them is indicated as 'allele 0', whereas the wild-type allele is indicated as 'allele A'. Rs7096206 is located in the promoter region, and it has been associated with modulation of MBL concentrations; the wild-type allele is classically indicated as 'Y', whereas the alternative is called 'X'. The statistical analysis in biallelic conditions was performed using a binomial glm model in R with the following covariates: age, sex, age × age, sex × age and ten principal components as already calculated for previous analyses.

To test the correlation between genetic variants and MBL concentrations, individuals were stratified based on the genotypes of the rs10824845 and/or the presence of at least one allele 0 in one of the rs5030737, rs1800450 or rs1800451 genotypes. Outliers were identified using the Rosner's test, and MBL plasma values >1.5 × interquartile range were excluded from the statistical analysis. Box–Cox transformation was used to normalize the data before applying further statistical analyses. ANOVA and *t*-tests were used to evaluate differences in MBL-transformed concentrations in different study groups.

Haplotype analysis was performed in two ways, including by (1) selecting relevant SNPs and using the hap-logistic option implemented in PLINK v.1.07 (ref. 68) and by (2) an unsupervised approach by means of the Beagle software v3.3 and 5.1 (<http://faculty.washington.edu/browning/beagle/b3.html>), which uses the method described by Browning and Browning⁶⁹ for inferring haplotype phase. In this case, we used the default setting of 1,000 permutations for calculating corrected *P* values.

In the meta-analysis, we took advantage of association data deposited in the Regeneron Genetic Center database (<https://rgc-covid19.regeneron.com/home>) for the GHS study (data available for 869 infected individuals and 112,862 healthy individuals of European ancestry). Pooled ORs and CIs were calculated using the Mantel–Haenszel model⁷⁰.

To test the role of rare variants in the susceptibility to a severe outcome, we analyzed data from Regeneron, focusing on the gene burden analysis in European cohorts considering the phenotype 'COVID-19-positive hospitalized versus COVID-19-negative or COVID-19 status unknown'. In the database, variants are grouped in four categories based on their predicted effect at the protein level and their frequency in the population. Missense variants are classified according to the prediction made by five algorithms (SIFT, PolyPhen2 HDIV, PolyPhen2 HVAR, LRT and Mutation Taster)³⁸. We focused on analysis of the most severe classes of variants: M1 (comprising only loss-of-function variants) and M3 (comprising loss-of-function and all the missense variants predicted as damaging by the five aforementioned algorithms) and on rare (MAF < 1%) as well as ultrarare (singleton) variants.

No statistical methods were used to predetermine sample sizes, but our sample sizes are similar to those reported in previous publications^{12,64,71}. For experiments with cells, randomization was not necessary, because all groups were derived from the same cell culture.

Reporting Summary. Further information on research design is available in the Nature Research Reporting Summary linked to this article.

Data availability

All data supporting the findings of this study are present in the main text and/or in the Supplementary Information. Additional data are available from the corresponding authors. For genetic studies, the dataset for infected individuals is publicly available at the European Bioinformatics Institute (www.ebi.ac.uk/gwas) under accession numbers GCST90000255 and GCST90000256 (ref. 12), whereas the dataset for healthy individuals is deposited in the Genotypes and Phenotypes database (<https://www.ncbi.nlm.nih.gov/gap/>) under the phs000294.v1.p1 accession code⁶⁵. Source data are provided with this paper.

References

- Bottazzi, B. et al. Multimer formation and ligand recognition by the long pentraxin PTX3. Similarities and differences with the short pentraxins C-reactive protein and serum amyloid P component. *J. Biol. Chem.* **272**, 32817–32823 (1997).
- Munthe-Fog, L. et al. The impact of FCN2 polymorphisms and haplotypes on the ficolin-2 serum levels. *Scand. J. Immunol.* **65**, 383–392 (2007).
- De Gasparo, R. et al. Bispecific IgG neutralizes SARS-CoV-2 variants and prevents escape in mice. *Nature* **593**, 424–428 (2021).
- Consortium, T. U. UniProt: the universal protein knowledgebase in 2021. *Nucleic Acids Res.* **49**, D480–D489 (2020).
- Sheriff, S., Chang, C. Y. & Ezekowitz, R. A. B. Human mannose-binding protein carbohydrate recognition domain trimerizes through a triple α -helical coiled-coil. *Nat. Struct. Biol.* **1**, 789–794 (1994).
- Berisio, R., Vitagliano, L., Mazzarella, L. & Zagari, A. Crystal structure of the collagen triple helix model [(Pro-Pro-Gly)₁₀]₃. *Protein Sci.* **11**, 262–270 (2002).
- Ng, K. K. et al. Orientation of bound ligands in mannose-binding proteins. Implications for multivalent ligand recognition. *J. Biol. Chem.* **277**, 16088–16095 (2002).
- Casalino, L. et al. Beyond shielding: the roles of glycans in the SARS-CoV-2 spike protein. *ACS Cent. Sci.* **6**, 1722–1734 (2020).
- Fu, B. et al. ALMOST: an all atom molecular simulation toolkit for protein structure determination. *J. Comp. Chem.* **35**, 1101–1105 (2014).
- Cesana, D. et al. Uncovering and dissecting the genotoxicity of self-inactivating lentiviral vectors in vivo. *Mol. Ther.* **22**, 774–785 (2014).
- Stravalaci, M. et al. Control of complement activation by the long pentraxin PTX3: implications in age-related macular degeneration. *Front. Pharm.* **11**, 591908 (2020).
- Follenzi, A., Ailles, L. E., Bakovic, S., Geuna, M. & Naldini, L. Gene transfer by lentiviral vectors is limited by nuclear translocation and rescued by HIV-1 pol sequences. *Nat. Genet.* **25**, 217–222 (2000).
- Scudieri, P. et al. Association of TMEM16A chloride channel overexpression with airway goblet cell metaplasia. *J. Physiol.* **590**, 6141–6155 (2012).
- Clementi, N. et al. Combined prophylactic and therapeutic use maximizes hydroxychloroquine anti-SARS-CoV-2 effects in vitro. *Front. Microbiol.* **11**, 1704 (2020).
- Mycroft-West, C. J. et al. Heparin inhibits cellular invasion by SARS-CoV-2: structural dependence of the interaction of the spike S1 receptor-binding domain with heparin. *Thromb. Haemost.* **120**, 1700–1715 (2020).
- Myocardial Infarction Genetics Consortium et al. Genome-wide association of early-onset myocardial infarction with single nucleotide polymorphisms and copy number variants. *Nat. Genet.* **41**, 334–341 (2009).
- Taliun, D. et al. Sequencing of 53,831 diverse genomes from the NHLBI TOPMed Program. *Nature* **590**, 290–299 (2021).
- Chang, C. C. et al. Second-generation PLINK: rising to the challenge of larger and richer datasets. *Gigascience* **4**, 7 (2015).
- Purcell, S. et al. PLINK: a tool set for whole-genome association and population-based linkage analyses. *Am. J. Hum. Genet.* **81**, 559–575 (2007).
- Browning, S. R. & Browning, B. L. Rapid and accurate haplotype phasing and missing-data inference for whole-genome association studies by use of localized haplotype clustering. *Am. J. Hum. Genet.* **81**, 1084–1097 (2007).
- Mantel, N. & Haenszel, W. Statistical aspects of the analysis of data from retrospective studies of disease. *J. Natl Cancer Inst.* **22**, 719–748 (1959).
- Asselta, R., Paraboschi, E. M., Mantovani, A. & Duga, S. ACE2 and TMPRSS2 variants and expression as candidates to sex and country differences in COVID-19 severity in Italy. *Aging* **12**, 10087–10098 (2020).

Acknowledgements

This work was supported by a philanthropic donation by Dolce & Gabbana fashion house (to A.M., C.G. and E.V.), by the Italian Ministry of Health for COVID-19 (COVID-2020-12371640 to A.M. and C.G.), by the Italian Ministry of University and Research (to P.I.) and by the Department of Excellence project PREMIA (PREcision Medicine Approach: bringing biomarker research to clinic, to P.I.). We also thank the generous contribution of Banca Intesa San Paolo and AMAF Monza ONLUS and AIRCS for the unrestricted research funding. L.V. has received funding from the European Union's Horizon 2020 research and innovation programme under grant agreement number 101003650 and from SNF (Swiss National Science Foundation) grant 31003A_182270. This work was conducted in the framework of, and made possible by, the collective effort of the Humanitas COVID-19 Task Force (the members are listed in the Supplementary Note). This paper is dedicated to S. Duga, who passed on 10 November 2021 and gave a key contribution to the genetic section of this report.

Author contributions

A.M. and C.G. conceived the study in March 2021 and catalyzed the interaction between different institutions. C.G., E.V. and B.B. supervised the development of the effort. M. Stravalaci and I.P. conducted the core experimental work related to binding, antiviral

activity and complement activation. The genetic analysis was conducted by E.M.P. and was supervised by S.D. and R.A. A.D. performed the imaging analysis. M.P., L.V., M.M. and A.C. performed SPR analysis and modeling. S.N.M. performed the bioinformatic analysis. M.U., R.R., P.I., R.B.-O. and P. Garred provided essential tools and materials. E.S., M. Sironi, C.P., D.C., P. Gallina, N.P., V.C., N.C. and N.M. conducted complementary experiments.

Competing interests

A.M., C.G. and B.B. are inventors of a patent (EP20182181) on PTX3 and obtain royalties on related reagents. A.M., C.G., B.B. and E.V. are inventors of two patents (102021000002738 and EP21214373.9) on MBL. R.R. is a full-time employee of the GSK group of companies. The other authors declare no competing interests.

Additional information

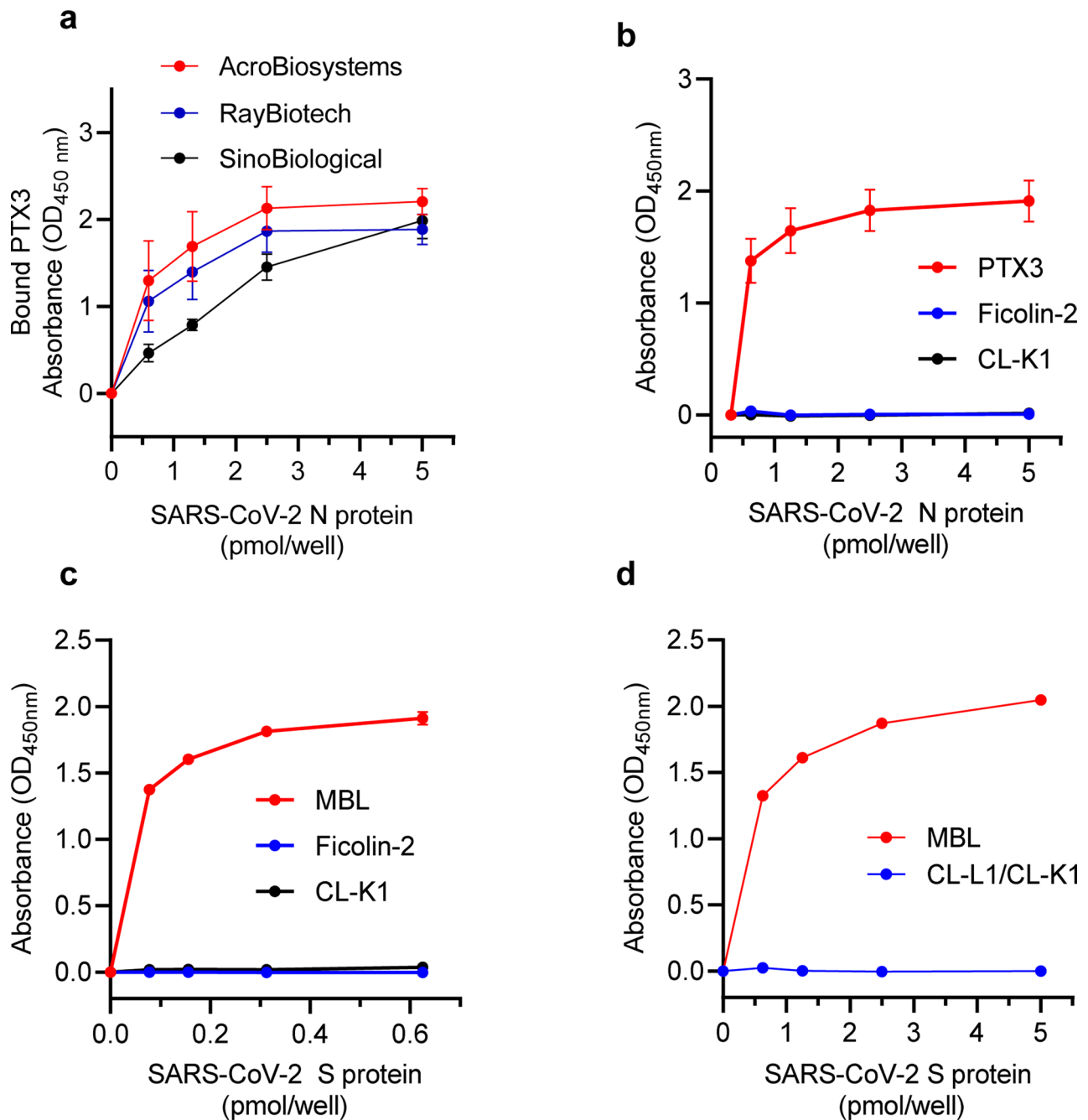
Extended data is available for this paper at <https://doi.org/10.1038/s41590-021-01114-w>.

Supplementary information The online version contains supplementary material available at <https://doi.org/10.1038/s41590-021-01114-w>.

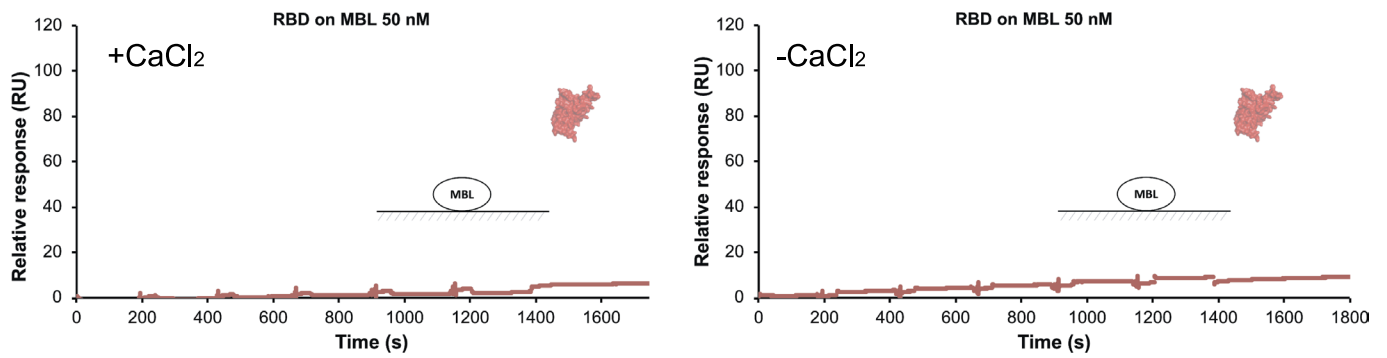
Correspondence and requests for materials should be addressed to Elisa Vicenzi, Alberto Mantovani or Cecilia Garlanda.

Peer review information *Nature Immunology* thanks Hideharu Sekine and the other, anonymous, reviewer(s) for their contribution to the peer review of this work. L.A. Dempsey was the primary editor on this article and managed its editorial process and peer review in collaboration with the rest of the editorial team.

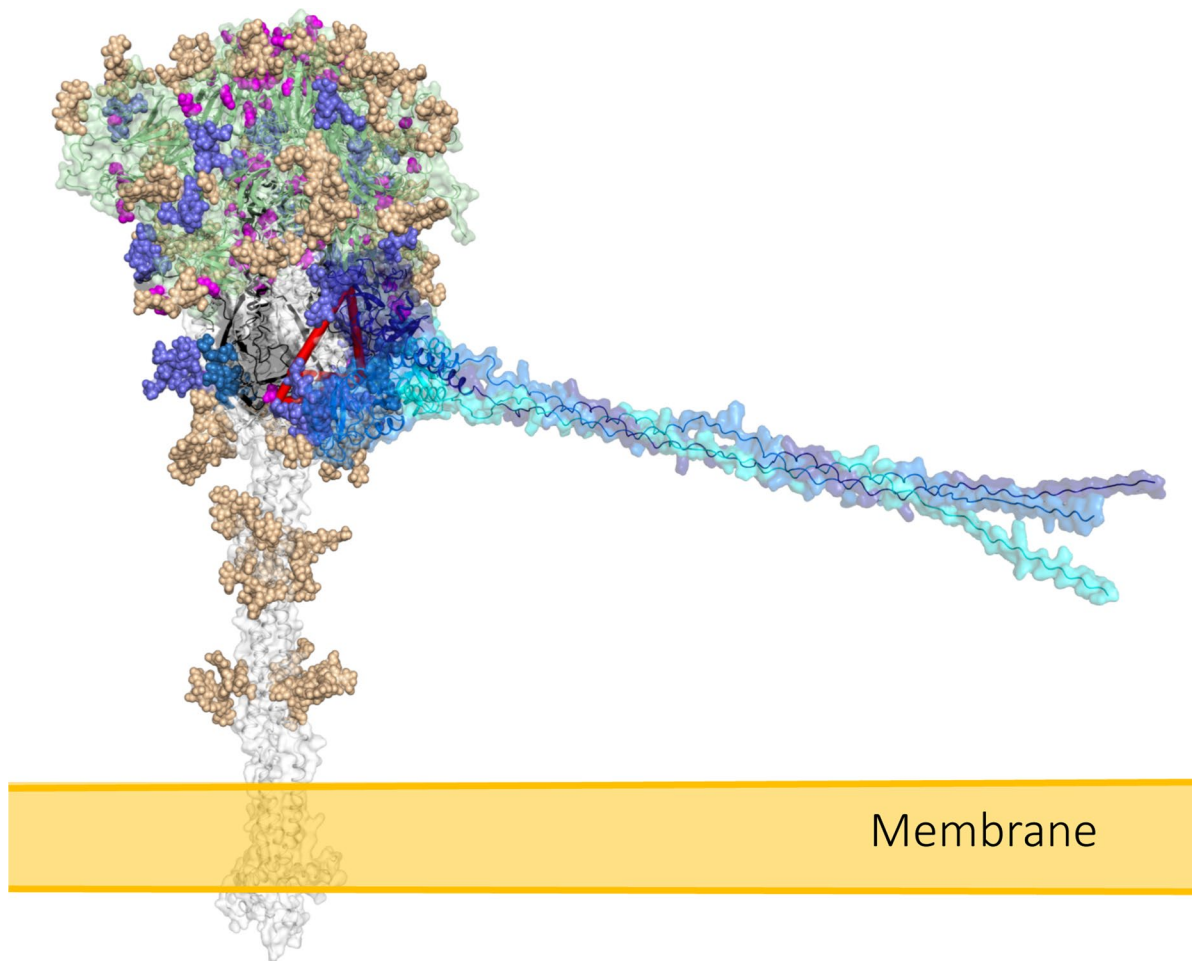
Reprints and permissions information is available at www.nature.com/reprints.



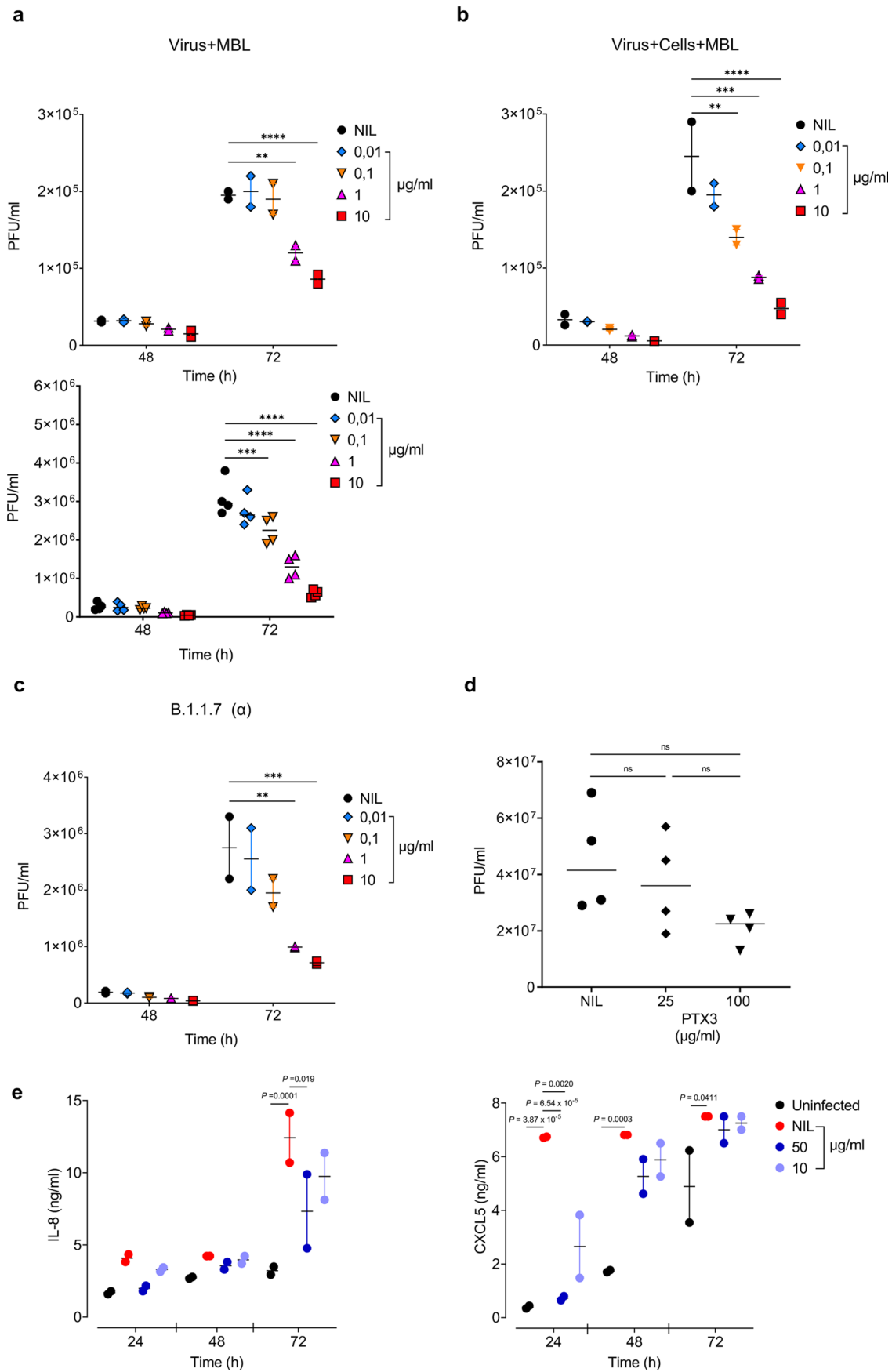
Extended Data Fig. 1 | Interaction between PRM and SARS-CoV-2 proteins. **a**) Binding of PTX3 to captured SARS-CoV-2 Nucleocapsid proteins from different companies. **b**) Binding of PTX3, Ficolin-2 and CL-K1 to SARS-CoV-2 N protein-coated plate. **c**) Binding of MBL, Ficolin-2 and CL-K1 to SARS-CoV-2 S protein-coated plate. **d**) Binding of MBL and CL-L1/CL-K1 heterocomplexes to SARS-CoV-2 S protein-coated plate. Data are presented as mean \pm SEM, $n=2$ (a, d) or $n=3$ independent experiments (b, c) performed in duplicate.



Extended Data Fig. 2 | SPR analysis of RBD and MBL interaction. Interaction between recombinant RBD and immobilized MBL in the presence or absence of calcium, as assessed by SPR analysis.



Extended Data Fig. 3 | A model for the Omicron Spike-MBL complex. Glycosylation sites are colored according to the oligomannose content: Gold < 60%. Purple > 80% up until S2' region. Blue > 80% in the S2' region. Omicron mutations are in magenta.



Extended Data Fig. 4 | See next page for caption.

Extended Data Fig. 4 | Inhibition of viral infection and chemokine production by MBL. (a-c) Inhibition of the infectivity of the D614G (a, b) and B.1.1.7 (α) (c) SARS-CoV-2 variants by MBL in Calu-3 cells. SARS-CoV-2 (a upper panel: MOI=0.1; b: MOI=0.1; c: MOI 0.01; a lower panel, MOI=1) was preincubated in complete medium containing different concentrations of MBL (0.01-10 μg/mL- 0.034-34 nM) before incubation with Calu-3 cells (Virus+MBL) (a), or both virus and cells were pre-incubated with the same concentrations of MBL (Virus+Cells+MBL) (b, c). After 48 and 72 h, the infectivity of SARS-CoV-2 present in cell culture supernatants was determined by a plaque-forming assay in Vero cells. NIL: no MBL. (d) SARS-CoV-2 production at the HBEC apical surface at 72 h PI, in the presence of 25 or 100 μg/ml (75 or 300 nM) PTX3. (e) Chemokine production by SARS-CoV-2 infected HBEC in the presence of MBL. Mean values, n=2 (a, b, d) or n=1 (c, e) independent experiments in duplicate cell culture are shown. (a, upper panel) **P=0.0011, ****P<0.001; (a, bottom panel) ***P=1.63×10⁻⁴, ****P<0.001; (b) **P=0.0027, ***P=1.35×10⁻⁴, ****P<0.001; (c) **P=0.0024, ***P=8.32×10⁻⁴ Statistical analysis was determined by two-way (a, b, c, e) or one-way (d) ANOVA, followed by Bonferroni's multiple comparison test.

Reporting Summary

Nature Portfolio wishes to improve the reproducibility of the work that we publish. This form provides structure for consistency and transparency in reporting. For further information on Nature Portfolio policies, see our [Editorial Policies](#) and the [Editorial Policy Checklist](#).

Statistics

For all statistical analyses, confirm that the following items are present in the figure legend, table legend, main text, or Methods section.

n/a Confirmed

- The exact sample size (n) for each experimental group/condition, given as a discrete number and unit of measurement
- A statement on whether measurements were taken from distinct samples or whether the same sample was measured repeatedly
- The statistical test(s) used AND whether they are one- or two-sided
Only common tests should be described solely by name; describe more complex techniques in the Methods section.
- A description of all covariates tested
- A description of any assumptions or corrections, such as tests of normality and adjustment for multiple comparisons
- A full description of the statistical parameters including central tendency (e.g. means) or other basic estimates (e.g. regression coefficient) AND variation (e.g. standard deviation) or associated estimates of uncertainty (e.g. confidence intervals)
- For null hypothesis testing, the test statistic (e.g. F , t , r) with confidence intervals, effect sizes, degrees of freedom and P value noted
Give P values as exact values whenever suitable.
- For Bayesian analysis, information on the choice of priors and Markov chain Monte Carlo settings
- For hierarchical and complex designs, identification of the appropriate level for tests and full reporting of outcomes
- Estimates of effect sizes (e.g. Cohen's d , Pearson's r), indicating how they were calculated

Our web collection on [statistics for biologists](#) contains articles on many of the points above.

Software and code

Policy information about [availability of computer code](#)

Data collection

no software was used

Data analysis

Confocal and STED super-resolution microscopy
Confocal images were processed, 3D rendered and analyzed with Leica Application Suite X software (LASX; version 3.5.5.19976)
STED images were de-convolved with Huygens Professional software (Scientific Volume Imaging B. V.; version 19.10)
Surface plasmon resonance analysis
Binding kinetics were determined by fitting of the experimental curves with the Langmuir 1:1 model according to standard procedures; data analyses were performed with Biacore™ Insight Evaluation Software v2.0.15.12933
Molecular modeling
The binding site of mannose molecules was determined aligning the MBL2 structure to the crystal structure of rat mannose protein A (PDB code 1KX1). Reference distances (~ 40 Å) between mannose molecules were computed in PYMOL (version 1.5.0.5, <https://pymol.org/2/>). Putative binding sites of MBL2 with SARS-CoV-2 were computed using the program ALMOST (version 2.2.0). Almost is available for the most common Unix-based operating systems, including Linux and Mac OS X. Almost is distributed free of charge under the GNU Public License, and is available both as a source code and as a binary executable from the project web site at <http://www.open-almost.org>.
Genetics
For genetic studies, case-control allele-dose association tests were performed using used for data plink (version 1.07 and version 1.9). Haplotype analysis was performed using beagle (version 3.3 and version 5.1) and R (version 4.5). All of them are freely available.
Statistical analysis
Prism GraphPad software (version 8.0, www.graphpad.com) and R (version 4.5, <https://www.r-project.org/>) were used for the statistical analyses.

For manuscripts utilizing custom algorithms or software that are central to the research but not yet described in published literature, software must be made available to editors and reviewers. We strongly encourage code deposition in a community repository (e.g. GitHub). See the Nature Portfolio [guidelines for submitting code & software](#) for further information.

Data

Policy information about [availability of data](#)

All manuscripts must include a [data availability statement](#). This statement should provide the following information, where applicable:

- Accession codes, unique identifiers, or web links for publicly available datasets
- A description of any restrictions on data availability
- For clinical datasets or third party data, please ensure that the statement adheres to our [policy](#)

All data supporting the findings of this study are present in the main text and/or in supplementary information. Additional data are available from the corresponding authors. For genetic studies, the dataset for cases is publicly available at the European Bioinformatics Institute (www.ebi.ac.uk/gwas) under accession numbers GCST90000255 and GCST90000256 [12], whereas the dataset for controls is deposited in the Genotypes and Phenotypes database (dbGaP; <https://www.ncbi.nlm.nih.gov/gap/>), under the phs000294.v1.p1 accession code [50].

Field-specific reporting

Please select the one below that is the best fit for your research. If you are not sure, read the appropriate sections before making your selection.

- Life sciences Behavioural & social sciences Ecological, evolutionary & environmental sciences

For a reference copy of the document with all sections, see [nature.com/documents/nr-reporting-summary-flat.pdf](https://www.nature.com/documents/nr-reporting-summary-flat.pdf)

Life sciences study design

All studies must disclose on these points even when the disclosure is negative.

Sample size

Sample size was not pre-determined by statistical analysis. In the infection experiments with the cell lines, three independent experiments in triplicate were performed, whereas with the human primary respiratory cells we obtained 3 independent donors which were sufficient to determine the permissivity to SARS-COV-2 infection, as in the infected untreated condition, viral titers increased by 4 log₁₀ from 24 h to 72 h post-infection.

For studies on human data, all available data were used and no calculation was performed on sample-size. In addition, our sample sizes are similar to those reported in previous publications^{12,65,71}.

Data exclusions

GraphPad Prism software was used to analyze the data. ROUT test or Rosner's test were applied to identify outliers. No outliers were identified and all data were included in the statistical analysis concerning Figures 1-5 and extended Data Figures 1, 2, 4. For Figure 6c and d, 3 outliers were excluded, based on Rosner's test.

Replication

Two-four experiments per type were performed with reproducible results. All replicates were used for the analysis.

Randomization

For experiments with cells, randomization was not necessary, since all groups derived from the same cell culture.

Blinding

For binding assays, IF and infection experiments, blinding was not considered relevant because the analysis was not operator-dependent.

Reporting for specific materials, systems and methods

We require information from authors about some types of materials, experimental systems and methods used in many studies. Here, indicate whether each material, system or method listed is relevant to your study. If you are not sure if a list item applies to your research, read the appropriate section before selecting a response.

Materials & experimental systems

- | n/a | Involvement | Involved in the study |
|-------------------------------------|-------------------------------------|-------------------------------|
| <input type="checkbox"/> | <input checked="" type="checkbox"/> | Antibodies |
| <input type="checkbox"/> | <input checked="" type="checkbox"/> | Eukaryotic cell lines |
| <input checked="" type="checkbox"/> | <input type="checkbox"/> | Palaeontology and archaeology |
| <input checked="" type="checkbox"/> | <input type="checkbox"/> | Animals and other organisms |
| <input type="checkbox"/> | <input checked="" type="checkbox"/> | Human research participants |
| <input checked="" type="checkbox"/> | <input type="checkbox"/> | Clinical data |
| <input checked="" type="checkbox"/> | <input type="checkbox"/> | Dual use research of concern |

Methods

- | n/a | Involvement | Involved in the study |
|-------------------------------------|--------------------------|------------------------|
| <input checked="" type="checkbox"/> | <input type="checkbox"/> | ChIP-seq |
| <input checked="" type="checkbox"/> | <input type="checkbox"/> | Flow cytometry |
| <input checked="" type="checkbox"/> | <input type="checkbox"/> | MRI-based neuroimaging |

Antibodies

Antibodies used

For ELISA binding assay and complement deposition assay the following primary antibodies were used: rabbit polyclonal IgG anti human PTX3 (produced in-house, Lot 23, 1:5000); rabbit polyclonal IgG anti-human C1q (Dako, Cat. A0136, Lot 20071886, 1:5000);

recombinant rabbit monoclonal IgG anti-human MBL (clone EPRI8381-156, Abcam, Cat. Ab190834, Lot GR3189741-3, 1:5000); mouse monoclonal IgG anti-human PTX2/SAP (clone 910119, R&D Systems, Cat. MAB1948, Lot CIVT0115061, 1:5000); rabbit polyclonal IgG anti-human CRP (Merck, Cat. 235752, Lot 3179228, 1:5000); rabbit polyclonal IgG anti-human SC5b-9 (Complementech, Cat. A227, Lot 5e, 1:2000); mouse monoclonal IgG anti-human CL-K1 (clone Hyb-15, 1:2000; produced in-house and provided by Peter Garred); mouse monoclonal IgG anti-human Ficolin-2 (clone FCN219, 1:2000; produced in-house and provided by Peter Garred). The following secondary antibodies were used: HRP-linked donkey anti-rabbit IgG (GE Healthcare, Cat. NA934V, Lot 12219044, 1:5000); HRP-linked sheep anti-mouse IgG (GE Healthcare, Cat. NA931V, Lot 16982037, 1:5000).

For confocal image analysis and STED super-resolution microscopy, the following primary antibodies were used: rabbit polyclonal IgG anti-SARS-CoV-2 Spike protein (Proteintech, Cat. 28867-1-AP, Lot 88993, 1:500); mouse monoclonal IgG anti-human Cytokeratine-14 (clone LL02, Pro-Sciences, Cat. 33-168, Lot 26009-2102, 1:200); rat monoclonal IgG anti-human MBL (clone 8G6, Hycult Biotech, Cat. HM1035, 1:100); rat monoclonal IgG anti-human MBL (clone 14D12, Hycult Biotech, Cat. HM1038, 1:100). The following secondary antibodies were used: donkey anti-rabbit IgG Alexa Fluor 488 (ThermoFisher Scientific, Cat. A-21206, 1:2000); donkey anti-rat IgG Alexa Fluor 594 (ThermoFisher Scientific, Cat. A-21209, 1:2000); donkey anti-mouse IgG Alexa Fluor 647 (ThermoFisher Scientific, Cat. A-31571, 1:2000).

Validation

Primary antibodies used for ELISA, binding assays, complement deposition assays and microscopy analysis are commercially available and validated by vendors for human proteins. References are reported for each of them in the manufacturer's website. Rabbit polyclonal IgG anti-human PTX3 was produced in-house by immunizing rabbits with recombinant human PTX3 and purified by immunoaffinity on PTX3-conjugated Sepharose-CNBr columns. The antibody was validated for ELISA in our laboratory (Brunetta et al., Nat. Immunology, 2021.(22)19-24). Mouse monoclonal IgG anti-human CL-K1 and anti-human Ficolin-2 were produced in-house and validated for ELISA (Bayarri-Olmos R et al., Front. Immunol. 9:2238. doi: 10.3389/fimmu.2018.02238; Munthe-Fog et al., Scand J Immunol. 2007 Apr;65(4):383-92).

Eukaryotic cell lines

Policy information about cell lines

Cell line source(s)

Eukaryotic cell lines:

Source:

Vero, BS CL101, Istituto Zooprofilattico, Brescia, Italy

Vero E6, ATCC CRL-1586

HEK-293T, ATCC CRL-3216

Calu-3, NovusPharma

Expi293F, cat A14527, ThermoFisher Scientific

Primary cells

Primary bronchial epithelial cells were isolated from mainstem human bronchi, derived from individuals undergoing lung transplant.

Authentication

Cells were verified by gene expression analysis. Species were confirmed by isozyme analysis (NP, G6PD, PEPB, MD and AST). Bronchial epithelial cells are not in the database of commonly misidentified cell lines.

Mycoplasma contamination

Cells in use in our laboratories are routinely check for mycoplasma contamination. Only mycoplasma-free cells were used.

Commonly misidentified lines (See ICLAC register)

No commonly misidentified cell lines were used in the study.

Human research participants

Policy information about studies involving human research participants

Population characteristics

For association analyses, we investigated a total of 2,000 individuals. These included: i) 332 patients with severe COVID-19, which was defined as hospitalization with respiratory failure and a confirmed SARS-CoV-2 viral RNA PCR test from nasopharyngeal swabs. Patients were recruited from intensive care units and general wards at two hospitals in the Milan area, i.e., the Humanitas Clinical and Research Center, IRCCS, in Rozzano, Italy (140 patients); and San Gerardo Hospital, in Monza, Italy (192 patients); ii) 1,668 controls from the general Italian population with unknown COVID-19 status. The analysis of MBL plasma levels was performed in a cohort of 40 patients. We included all males and non-pregnant females, 18 years of age or older, admitted to Humanitas Clinical and Research Center (Rozzano, Milan, Italy) between March and April, 2020 with a laboratory-confirmed diagnosis of COVID-19.

For all subjects, data about age and sex were collected, and used as covariates in the association analyses. All samples were genotyped using Affymetrix 6.0 GeneChip (data available at: Genotypes and Phenotypes database, dbGaP; <https://www.ncbi.nlm.nih.gov/gap/>, under the phs000294.v1.p1 accession code) or the Illumina Global Screening Array (data available at: the European Bioinformatics Institute, www.ebi.ac.uk/gwas under accession numbers GCST90000255 and GCST90000256). An extensive quality control step was performed before proceeding with the imputation process. In the post-imputation steps, we only retained those SNPs with $R^2 \geq 0.6$ and minor allele frequency (MAF) $\geq 1\%$, and considered for the downstream association analysis only those SNPs localized in the MBL2 region (the gene +/-500 kb). The final set of analyzed variants comprised 3,425 SNPs.

HEBC isolation. The UOC Genetica Medica of the IRCCS Istituto Giannina Gaslini houses a large collection of primary bronchial cells banked as frozen aliquots in the frame of the Primary Bronchial Cell Repository supported by the Italian Cystic Fibrosis Foundation. Epithelial cells are obtained from mainstem human bronchi, derived from individuals undergoing lung transplant. Among the donors there are subjects undergoing lung transplantation for pathologies like cystic fibrosis, emphysema, pulmonary hypertension, idiopathic fibrosis, sarcoidosis, bronchiectasis, COPD, alpha-1 antitrypsin deficiency or surfactant dysfunction. For the present study, primary cells from 3 individuals were chosen: BE37: 67-yr male; emphysema

BE63: 63-yr old female; idiopathic fibrosis
BE177: 64-yr old male; idiopathic fibrosis

Recruitment

Cases are all characterized by a severe form of COVID-19, defined as hospitalization with respiratory failure. This comprises the use of oxygen supplementation or mechanical ventilation (supplemental oxygen therapy only, noninvasive ventilatory support, invasive ventilatory support, or extracorporeal membrane oxygenation). Information about the SARS-CoV-2 infection status in the control participants is not known, however this concern is mitigated by the fact that the presence of susceptible persons in the control group would only bias the tests toward the null.

Ethics oversight

Approvals for the project were obtained from the relevant ethics committees (Humanitas Clinical and Research Center, reference number, 316/20; the University of Milano-Bicocca School of Medicine, San Gerardo Hospital, reference number, 84/2020). Written informed consent was obtained from the study patients at each center. The collection of bronchial epithelial cells and their study to investigate airway epithelium physiopathology were specifically approved by the Ethics Committee of the Istituto Giannina Gaslini following the guidelines of the Italian Ministry of Health (registration number: ANTECER, 042-09/07/2018). Each patient provided informed consent to the study using a form that was also approved by the Ethics Committee. Viral isolation from clinical samples and use for research purposes was approved by San Raffaele Hospital IRB within the COVID-19 Biobanking project "COVID-Biob" (34 /int/2020 19/March/2020. ClinicalTrials.gov Identifier: NCT04318366). Each patient provided informed consent.

Note that full information on the approval of the study protocol must also be provided in the manuscript.